JGR Solid Earth

RESEARCH ARTICLE

10.1029/2025JB031421

Refining 3D Displacement Fields and Coseismic Slip Models of the 2023 Kahramanmaraş Earthquakes Using Subswath and Burst Overlap Interferometry (SBOI)

Muhammet Nergizci[1], Milan Lazecky[1], Tim J. Wright[1], Andrew Hooper[1], Qi Ou[1,2], Christophe Magnard[3], and Ziyadin Çakir[4]

[1]COMET, School of Earth and Environment, University of Leeds, Leeds, UK, [2]Global Change Institute, School of GeoSciences, University of Edinburgh, Edinburgh, UK, [3]Gamma Remote Sensing AG, Gümligen, Switzerland, [4]Istanbul Technical University, Istanbul, Türkiye

Key Points:

- Subswath and Burst Overlap Interferometry (SBOI) enhances 3D displacement field resolution, particularly in regions with significant north-south deformation
- SBOI improves the constraint on coseismic slip inversion, refining slip estimates while significantly decreasing uncertainties
- SBOI data enable detailed near-field deformation analysis in areas where traditional InSAR/SAR methods fail

Supporting Information:

Supporting Information may be found in the online version of this article.

Correspondence to:

M. Nergizci,
eemne@leeds.ac.uk

Citation:

Nergizci, M., Lazecky, M., Wright, T. J., Hooper, A., Ou, Q., Magnard, C., & Çakir, Z. (2025). Refining 3D displacement fields and coseismic slip models of the 2023 Kahramanmaraş earthquakes using subswath and burst overlap interferometry (SBOI). *Journal of Geophysical Research: Solid Earth*, *130*, e2025JB031421. https://doi.org/10.1029/2025JB031421

Received 25 FEB 2025
Accepted 4 NOV 2025

Author Contributions:

Conceptualization: Tim J. Wright, Andrew Hooper
Formal analysis: Muhammet Nergizci
Investigation: Muhammet Nergizci
Methodology: Muhammet Nergizci, Tim J. Wright, Andrew Hooper
Software: Muhammet Nergizci, Milan Lazecky, Tim J. Wright, Andrew Hooper, Qi Ou, Christophe Magnard
Supervision: Tim J. Wright, Andrew Hooper
Validation: Milan Lazecky, Tim J. Wright, Andrew Hooper, Qi Ou, Christophe Magnard, Ziyadin Çakir

Abstract The 6 February 2023 Kahramanmaraş Earthquakes caused extensive deformation along the East Anatolian Fault Zone, producing significant north-south displacements. Standard Interferometric Synthetic Aperture Radar (InSAR) methods face significant challenges in resolving near-field deformation due to phase decorrelation caused by high displacement gradients. This study demonstrates the capability of Subswath and Burst Overlap Interferometry (SBOI), which leverages all possible overlap regions of Sentinel-1 TOPS mode to retrieve along-track deformation and improve the resolution of 3D displacement fields. We introduce an enhanced methodology that calculates pixel-based scaling factors for spectral separation, enabling accurate deformation measurements in both burst and subswath overlap regions. Although overlap regions are spatially discontinuous and cover only ∼10% of the frame, SBOI offers critical constraints that complement conventional SAR, enabling full spatial coverage. We combine SBOI with azimuth and range offsets to produce 3D displacement fields and perform unsmoothed Bayesian slip inversion. Results reveal significant improvements in constraining north-south deformation, reducing residuals, and decreasing uncertainties in the slip inversion model compared to solutions without SBOI. Linear regression analysis between solutions with and without SBOI demonstrates ∼40% reduction in RMS error for the north-south component of 3D displacement field. Near-field SBOI profiles also capture detailed deformation gradients along fault ruptures, offering insights into fault kinematics and rupture dynamics. This study highlights SBOI as a powerful tool for resolving high-gradient deformations and enhancing 3D displacement fields and geodetic slip models, particularly in regions experiencing large coseismic deformation with significant north-south components, where conventional InSAR and SAR measurements are insufficient.

Plain Language Summary Earthquakes cause the ground to move in different directions, but it is difficult to measure movement from north to south using current Interferometric Synthetic Aperture Radar data from spaceborne missions. This limits our ability to create accurate 3D maps of how the ground shifts during earthquakes using satellite-based methods. In this study, we combined offset tracking data set with an advanced processing technique called Subswath and Burst Overlap Interferometry that takes advantage of overlapping areas in satellite radar images from the European Sentinel-1 satellites to better measure north-south movement. We applied this method to the 2023 Kahramanmaraş earthquakes in Türkiye, which caused complex ground deformation. Our results show that this technique improves how well we can measure ground movement in the north-south direction and leads to better models of how the fault slipped during the earthquakes. We have made this method available through an open platform so that other researchers can use it to study earthquakes and related hazards around the world.

1. Introduction

Spaceborne Interferometric Synthetic Aperture Radar (InSAR) is extensively used in tectonic studies to measure deformation of the Earth's crust arising from coseismic slip, interseismic loading, postseismic relaxation, volcanic unrest, and other geophysical phenomena (Biggs & Wright, 2020; Bürgmann et al., 2000; Elliott et al., 2016; Hu et al., 2014). InSAR measurements are obtained in the line-of-sight (LoS) direction, capturing surface deformation as movement toward or away from the satellite along this vector. Due to the near-polar orbits and side-looking geometry of SAR satellites, the LoS vector is highly sensitive to vertical and east-west components of surface displacement but is significantly limited in resolving north-south deformation.

Visualization: Muhammet Nergizci
Writing – original draft:
Muhammet Nergizci
Writing – review & editing:
Muhammet Nergizci, Milan Lazecky, Tim J. Wright, Andrew Hooper, Qi Ou, Christophe Magnard, Ziyadin Çakir

Current Earth observation SAR missions from various agencies, such as the European Space Agency's (ESA) Sentinel-1 (S-1), the Japan Aerospace Exploration Agency's (JAXA) ALOS-PALSAR, and the Canadian Space Agency's (CSA) RADARSAT, typically utilize right-looking geometries and operate with similar orbital inclinations of approximately 98°. These configurations allow for consistent revisit times and global coverage between latitudes 80°S and 80°N. However, this design poses challenges in decomposing LoS measurements into true 3D displacement components, as observations are restricted to just two geometries: ascending and descending passes. Even with combined data from multiple satellite missions, accurately resolving the north-south deformation remains challenging (Wright et al., 2004).

New SAR missions address these limitations by providing both left- and right-looking capabilities such as ALOS-2, RADARSAT-2, and NASA-ISRO (National Aeronautics and Space Administration and Indian Space Research Organisation)'s NISAR, which is dedicated to left-looking geometry (Morishita & Kobayashi, 2022; Rosen & Kumar, 2021; Samsonov & Jiang, 2024). However, the near-polar orbits with similar inclinations of these missions still limit the ability to fully capture north-south deformation, which remains relatively poor compared to the vertical and east-west components (Wright et al., 2004). Furthermore, the lack of temporal synchronisation between different satellite missions complicates efforts to observe deformation during the same time period, hindering the ability to measure consistent displacement magnitudes or isolate unrelated deformation sources.

To enhance azimuth displacement sensitivity, advanced SAR missions are incorporating novel acquisition modes. For example, Yague-Martinez, Prats-Iraola, Wollstadt, and Moreira (2019) demonstrated the effectiveness of a two-look burst acquisition mode in TerraSAR-X, significantly improving azimuth displacement sensitivity to millimeter-level precision and overcoming the limitations of standard ScanSAR and TOPS (Terrain Observation by Progressive Scans) modes. Similarly, ESA's proposed ROSE-L mission, scheduled for launch in 2028, aims to integrate this two-look burst acquisition mode to enhance azimuth displacement observations (Perna et al., 2024; Trumpf et al., 2025). Furthermore, ESA's Harmony mission, set for launch in 2030, is designed to operate alongside Sentinel-1 with two companion satellites, addressing the limitations of LoS diversity and enabling the retrieval of full 3D displacement fields (López-Dekker et al., 2021; Pappas et al., 2025). However, until these missions become operational, SAR systems alone remain insufficient for accurately constraining north-south deformation. Researchers often rely on dense Global Navigation Satellite System (GNSS) networks to supplement InSAR observations. GNSS data effectively constrain north-south deformation in regions with sufficient station density, while east-west and vertical components are typically resolved using ascending and descending LoS geometries. In some cases, north-south deformation is assumed to be negligible in areas dominated by large east-west or vertical deformation, or it is indirectly inferred by combining these components (Hussain et al., 2018; Ou et al., 2022; Shen et al., 2024; Weiss et al., 2020).

Alternative techniques, such as Azimuth Offset Tracking (AOT), Spectral Diversity Method, and Burst Overlap Interferometry (BOI), have been employed to address the gaps in north-south deformation observations. These methods derive 3D displacement fields from SAR data in regions affected by earthquakes, volcanic eruptions, and other geophysical events, complementing standard InSAR measurements (Fialko et al., 2001; Funning et al., 2005; Fielding et al., 2013; He et al., 2019a; J. Liu, Hu, Li, Ma, Shi, et al., 2022).

The Offset Tracking method measures displacement in both range and azimuth directions through cross-correlation of intensity data (Michel et al., 1999). This method is less impacted by phase decorrelation near fault zones and does not require a phase unwrapping step. However, its accuracy depends on the pixel size of the satellite system. For S-1 TOPS data, the method achieves meter-level accuracy in the azimuth direction due to the relatively coarse azimuth pixel spacing of ~14 m (He et al., 2019a; Merryman & Peter, 2019; L. Xu et al., 2021).

The Spectral Diversity Method, also referred to as Multiple Aperture Interferometry (MAI), is a technique for retrieving azimuthal displacement from SAR phase information by employing double differencing between two split-beam interferograms (Scheiber & Moreira, 2000). Initially developed to estimate misregistration between interferometric pairs under non-deformation scenarios, this method has been extended to deformation scenarios following the coregistration process (Bechor & Zebker, 2006; Jung et al., 2014). It leverages the spectral separation of SAR data by dividing the raw image spectrum into upper and lower spectral sub-bands. Double-difference interferograms are then generated from these sub-bands, enabling the estimation of azimuthal displacements.

Instead of splitting the spectral bandwidth, Prats-Iraola et al. (2012) proposed the Enhanced Spectral Diversity (ESD) method, which takes advantage of the natural spectral gap between bursts in the burst overlap regions, for the coregistration of interferogram pairs in TOPS acquisition mode to achieve a more precise estimation of misregistration errors. These regions naturally provide two acquisitions with different geometries (backward- and forward-looking) due to the different squint angles in the azimuth direction (Figure 1). This acquisition geometry results in inherently high spectral separation within the overlap areas, which is nearly 20 times larger than that achieved using the standard Spectral Diversity Method. This enhanced separation can be used to significantly improve the coregistration of interferogram pairs, minimizing phase jumps along the azimuth direction (Figure 6 in Prats-Iraola et al. (2012); see also Rodriguez-Cassola et al. (2014) for additional corrections required for TOPS mode). The ESD method has also been extended for deformation extraction in the azimuth direction. If the interferogram pairs are well-aligned during the coregistration step (Yague-Martinez, Prats-Iraola, Wollstadt, & Moreira, 2019), the double-difference interferograms in burst overlap regions can be used to extract azimuth displacement with enhanced sensitivity, capturing both surface deformation and ionospheric effects. In non-deformation scenarios, phase information from ESD in burst-overlap regions can be used to extract ionospheric effect by leveraging the dispersive nature of the ionosphere, a technique known as the split-spectrum method (Gomba et al., 2016; C. Liang et al., 2019; Piromthong & Hooper, 2025). In deformation scenarios, where azimuth shifts are typically driven by ground displacement, this technique is referred to as Burst Overlap Interferometry (BOI) and is used to capture the north-south deformation (Grandin et al., 2016).

Several studies in the literature have demonstrated that BOI can be utilized to constrain north-south displacements within 3D displacement fields, and they have shown its significant contributions to slip inversion studies in coseismic events, outperforming both AOT and MAI despite its sparse nature in overlap regions (Cui et al., 2022; He et al., 2019b; H. Jiang et al., 2017; J. Liu, Hu, Li, Ma, Wu, et al., 2022; L. Xu et al., 2021). Furthermore, BOI time-series analysis has achieved millimeter-level accuracy, making it well-suited for detecting small tectonic deformations such as postseismic and interseismic displacements (X. Li et al., 2021, 2024; Magen, Baer, Ziv, Inbal, & Nof, 2024; Yague-Martinez, Prats-Iraola, Pinheiro, & Jaeger, 2019).

Despite the advantages of BOI, several challenges and opportunities for improvement remain. A critical gap lies in the accurate calculation of spectral separation within BOI overlap regions, which varies non-uniformly in the range and azimuth directions due to platform movement. Accurate accounting for spectral separation is essential for determining true deformation magnitudes and converting phase changes from radians to meters. Furthermore, BOI has traditionally focused on overlap regions between adjacent bursts within the same subswath, often neglecting inter-subswath overlap regions in the range direction. These inter-subswath overlaps, which also exhibit spectral separation, represent an underutilized opportunity to obtain azimuth displacements. Expanding BOI to incorporate these regions, a method we term Subswath and Burst Overlap Interferometry (SBOI), can maximize the utility of overlap areas, increase spatial coverage, and enhance the extraction of north-south deformation from S-1 TOPS data (Hooper & Spaans, 2016; H. Jiang et al., 2017; Spaans, 2016).

Another challenge with BOI lies in phase unwrapping, where a single phase cycle (2π or one fringe) corresponds to approximately 150 cm of azimuth displacement. While previous events did not produce such large azimuthal displacements, the 2023 Kahramanmaraş Earthquakes presented an unprecedented case study with significant deformation gradients. This event serves as an ideal opportunity to address critical gaps in SBOI and to evaluate its capabilities.

On 6 February 2023, two devastating earthquakes struck Türkiye within a 9-hr interval along the East Anatolian Fault (EAF) zone, a major tectonic boundary accommodating the relative motion between the Anatolian microplate and the Arabian plate (Figure 2). Previous geodetic and seismological studies (C. Liu et al., 2023; Melgar et al., 2023; Zhang et al., 2023) indicate that the Mw 7.8 earthquake nucleated on the Narlı Fault, a branch of the Dead Sea Fault (DSF) (Emre et al., 2018; Güvercin et al., 2022), and propagated approximately 25 km northeast to reach the EAF at the Pazarcık segment. The rupture then expanded bilaterally, propagating northward and southward along the Pazarcık segment. To the north, the rupture extended through the Erkenek segment before terminating at the Pütürge segment (Barbot et al., 2023; Lomax, 2023; Zhang et al., 2023). To the south, it propagated beyond the Pazarcık segment into the Amanos segment, rupturing it before halting southwest of the Amik Basin, where the EAF intersects the DSF. Ultimately, the Mw 7.8 earthquake resulted in a rupture length of approximately 350 km, affecting three major segments of the EAF. The Mw 7.6 earthquake nucleated on the Çardak Fault and propagated bilaterally, extending westward to the Savrun Fault. In the east, the rupture initially

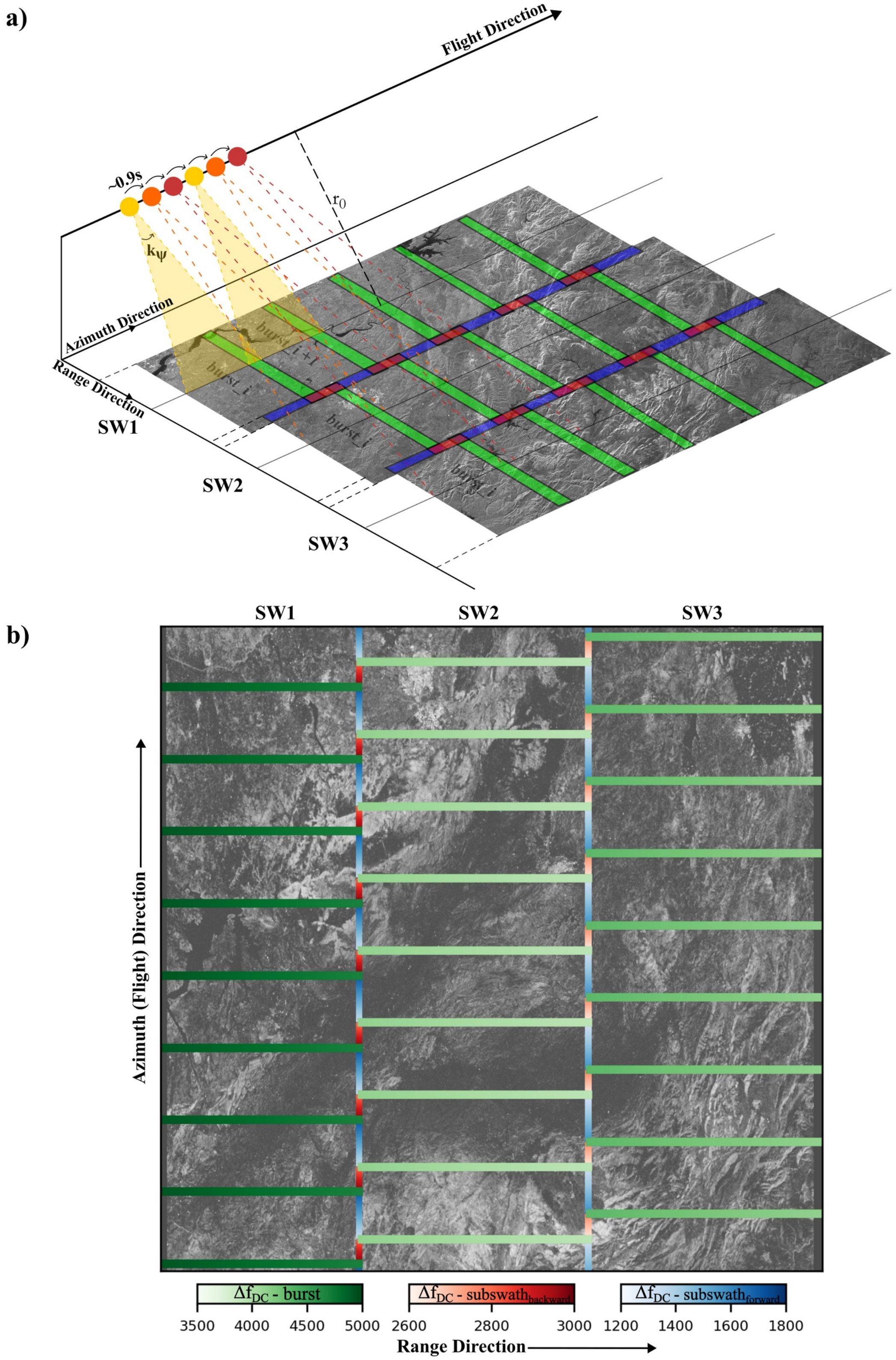

Figure 1. Spectral diversity variations and S-1 TOPS acquisition mode. (a) Illustration of the S-1 TOPS acquisition mode, highlighting subswath and burst overlaps. (b) Spectral diversity variations in burst overlaps, backward and forward of subswath overlaps are shown in green, red, and blue, respectively.

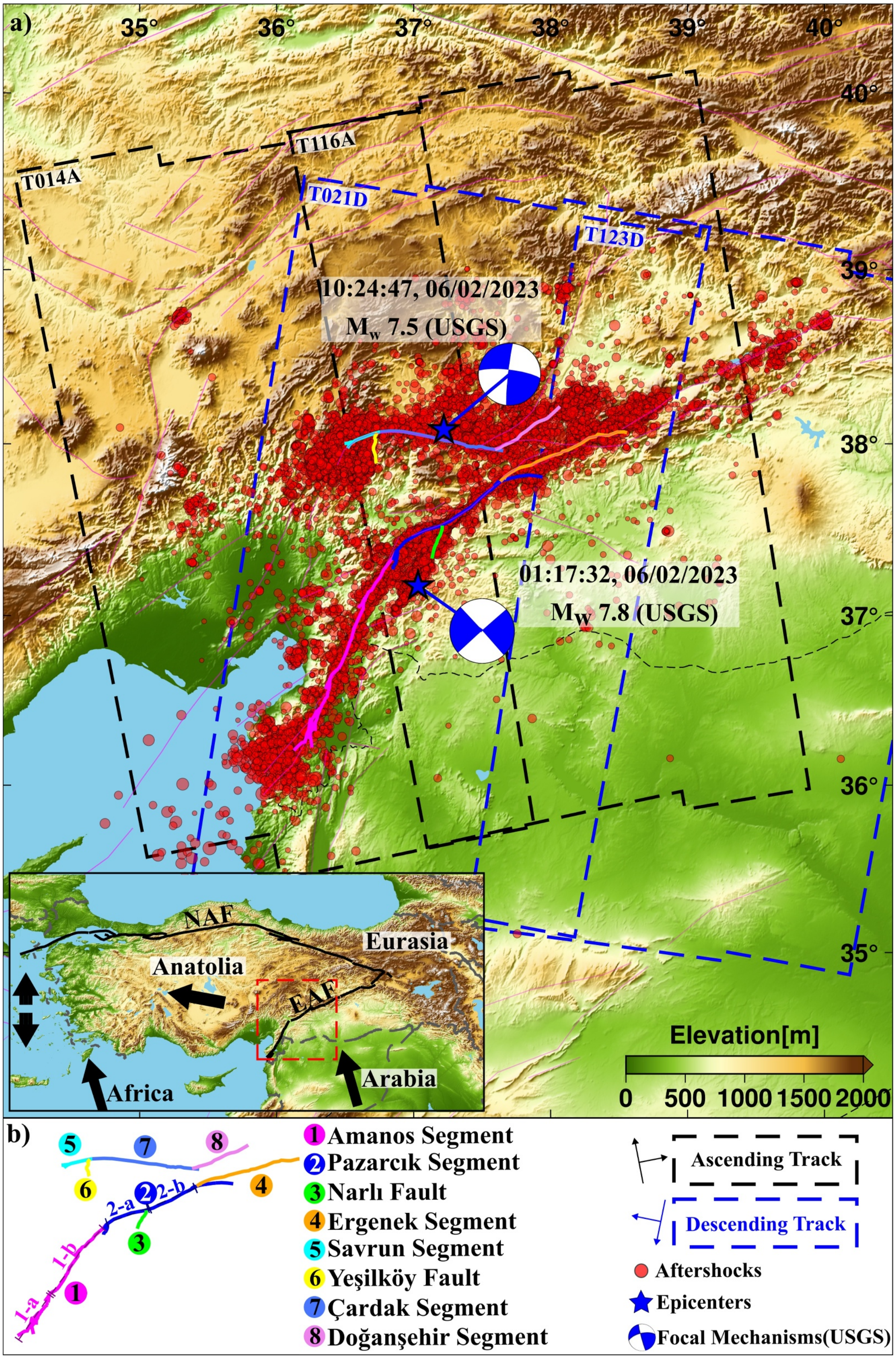

Figure 2. Study region of the Kahramanmaraş Earthquakes. (a) The area of interest is shown in the inset map. The black dashed rectangles represent the ascending tracks, while the blue dashed rectangles indicate the descending tracks of Sentinel-1 (S-1). The blue stars and focal mechanisms mark the epicenters of the earthquakes (USGS, 2023), and the red dots represent the aftershocks (Lomax, 2023). The colored lines indicate different segments of the total ruptures caused by the earthquakes. (b) Explanation of the colors corresponding to the segment names.

propagated along the Sürgü Fault but did not continue along its full length. Instead, the rupture jumped to the Doğanşehir Fault and continued northeastward, propagating between the Malatya Fault and the Sürgü Fault. The total rupture length of this event was approximately 150 km. These earthquakes rank among the most catastrophic in modern Türkish history, resulting in over 60,000 fatalities across Türkiye and Syria (Hussain et al., 2023).

The Kahramanmaraş Earthquakes generated significant north-south displacements along the EAF with total offsets of up to 4 m. This surpasses the displacement observed in previous S-1 era events, such as the 2016 Kumamoto, 2017 Ezgeleh, and 2019 Ridgecrest earthquakes, where offsets were limited to the decimeter-to-meter scale (He et al., 2019b; H. Jiang et al., 2017; Magen, Baer, Ziv, Inbal, & Nof, 2024).

This study aims to fully exploit the potential of SBOI by incorporating both burst and subswath overlap regions in S-1 TOPS mode data to analyze the Kahramanmaraş Earthquakes, which exhibit significant north-south deformation over a wide area. We introduce an improved methodology for calculating pixel-based scaling factors to ensure accurate deformation measurements, with the processing framework integrated into the COMET-LiCS (Center for the Observation and Modeling Earthquake, Volcanoes, and Tectonics-Looking into the Continents) system (Lazeckỳ et al., 2023). By combining SBOI with S-1 pixel offset tracking data sets, we generate a comprehensive 3D displacement field. We then evaluate the impact of SBOI on slip inversion methodologies, and conduct a detailed analysis of near-field deformation. Comparative analyses using GNSS and different combinations of the SAR-derived data sets reveal unique ability of SBOI to improve geodetic analyses, highlighting its potential for advancing future tectonic and seismic studies.

2. Sentinel-1 TOPS Data

2.1. Subswath and Burst Overlap Interferometry

While the initial applications of TOPS were demonstrated with TerraSAR-X (Meta et al., 2009; Prats-Iraola et al., 2012; Scheiber et al., 2010) and RADARSAT-2 (Davidson et al., 2013; Geudtner, 2014), Sentinel-1 is the first constellation to use Terrain Observation by Progressive Scans (TOPS) as its standard acquisition mode. In TOPS mode, radar images are acquired in bursts that overlap in both the azimuth and range directions, ensuring complete image coverage. These overlap regions contain two different LoS vectors at different Doppler frequencies due to the different squint angles in the along-track direction, resulting in spectral separation within these areas (Figure 1). This configuration enables the monitoring of along-track deformation through a method known as Burst Overlap Interferometry (BOI), which applies double-difference interferograms between different viewing geometries (Grandin et al., 2016).

BOI has become a widely used approach in the literature for extracting north–south deformation at centimeter-to millimeter-scale precision from InSAR data, and has been shown to offer significantly higher accuracy than azimuth offset tracking and multiple aperture InSAR for Sentinel-1 data. Consequently, it has been applied in time series analyses of postseismic (Magen, Baer, Ziv, Inbal, & Nof, 2024; Yague-Martinez, 2020), interseismic (X. Li et al., 2021, 2024; Ma et al., 2022), and coseismic studies (Cui et al., 2022; Grandin et al., 2016; He et al., 2019b; H. Jiang et al., 2017; J. Liu, Hu, Li, Ma, Wu, et al., 2022; Ma et al., 2024).

In coseismic cases such as the 2016 Mw 7.0 Kumamoto earthquake (H. Jiang et al., 2017), 2017 Mw 7.3 Ezgeleh earthquake (He et al., 2019b), and 2020 Mw 6.5 Monte Cristo Range earthquake (Cui et al., 2022), BOI was used to retrieve azimuth displacements and assess contributions to 3D displacement fields and slip inversion. These studies demonstrated that BOI improved slip models, when combined with SAR/InSAR data. However, in these events, the deformation captured in burst overlaps generally remained below the BOI phase ambiguity threshold (∼0.8 m), allowing measurements without significant unwrapping challenges. Additionally, BOI coverage typically spanned areas of ∼100 × 100 km or smaller.

While H. Jiang et al. (2017) also examined subswath overlaps, these regions were located far from the main deformation zone of the Kumamoto earthquake and were not included in the analysis or used to inform the slip inversion. Similarly, Spaans (2016) presented deformation signals from burst and subswath overlaps during the 2015 Mw 8.3 Illapel earthquake, but the displacements in overlap regions did not exceed the phase ambiguity threshold, limiting the evaluation of sensitivity differences between overlap types.

In most of the literature, BOI refers specifically to double-difference interferograms formed in burst overlap regions along the azimuth direction. Overlaps in the range direction, which we will refer to as subswath overlaps,

Table 1
Parameters for SW1, SW2, SW3 of S-1 TOPS Mode

Parameters	SW1	SW2	SW3
Antenna steering rate (s^{-1})	−1.59°	−0.98°	−1.397°
Near range (m)	799,425	845,877	901,474
Center range (m)	825,327	876,250	930,739
Far range (m)	851,229	906,623	960,005
Platform velocity (m/s)		7593.905	
Burst time difference T_{diff} (s)		2.758	
$\Delta f_{\mathrm{DC,near}}$ (Hz)	4,916	4,124	4,336
$\Delta f_{\mathrm{DC,center}}$ (Hz)	4,793	4,022	4,227
$\Delta f_{\mathrm{DC,far}}$ (Hz)	4,676	3,925	4,124
Phase cycle$_{\mathrm{near}}$ (m)	1.381	1.647	1.566
Phase cycle$_{\mathrm{center}}$ (m)	1.417	1.688	1.606
Phase cycle$_{\mathrm{far}}$ (m)	1.452	1.730	1.647
	T_{diff} (s)	Δf_{DC} (Hz)	Phase cycle (m)
BOI	~2.76	~4,800	~1.42
SOI$_{bwr}$	~−1.80	~2,900	~2.35
SOI$_{fwr}$	~0.96	~1,500	~4.54

Note. Spectral separations of overlaps[a]. [a]Spectral separation in overlaps is calculated for the center slant range/azimuth time of the overlap areas in SW1.

are typically not used for along-track deformation. These overlaps account for approximately 1.7% of the imaged area. By incorporating subswath overlaps alongside burst overlaps, the total along-track deformation coverage increases to about 10.3% of the scene (Brcic et al., 2014).

In this study, we extend BOI by systematically integrating both burst and subswath overlaps within regions of significant deformation and by deriving pixel-based scaling factors that account for spatial variations in spectral separation. Accurate calculation of Doppler frequency separation is essential for converting phase to displacement at millimeter precision. Even within burst overlap regions, spectral separation varies from near to far range, and it differs between subswaths due to changes in slant range (Table 1). Therefore, we calculate pixel-based scaling factors for both burst and subswath overlaps and test their sensitivity in regions where these overlaps are adjacent. The 2023 Kahramanmaraş earthquake provides a valuable opportunity to assess this method, as it produced a large and complex deformation field spanning approximately ~300 × 300 km with along-track offsets reaching up to 4 m, which is much larger and more complex than in prior BOI studies (Cui et al., 2022; Grandin et al., 2016; He et al., 2019b; H. Jiang et al., 2017).

The Doppler frequency separation, Δf_{DC}, in the overlap region arises from two primary factors: (a) the platform's movement, which defines the classical Doppler rate of the target, K_a, and (b) beam steering in the azimuth direction, which induces an additional Doppler rate component, K_{rot}, calculated as follows (Prats-Iraola et al., 2012):

$$\Delta f_{DC} = \frac{K_a K_{rot}}{K_a - K_{rot}} T_{diff}; K_a = -\frac{2v_s^2}{\lambda R_0}; K_{rot} \simeq \frac{2v_s}{\lambda} k_\psi \tag{1}$$

where T_{diff} represents the timing difference between burst acquisitions, v_s denotes the effective satellite velocity, R_0 is the range distance (slant range) from the target to the satellite, and λ is the wavelength. The term k_ψ corresponds to the antenna beam steering rate.

The along-track displacement in overlap areas Δx_{ovl} can be expressed as (Scheiber & Moreira, 2000):

$$\Delta x_{ovl} = \frac{\Delta \phi_{ovl} PRF}{2\pi \Delta f_{DC}} r_{azi} \tag{2}$$

where $\Delta \phi_{ovl}$ is the double-difference interferogram phase, $PRF = 486.486$ Hz is the Pulse Repetition Frequency, and r_{azi} denotes the azimuth pixel size of S-1 TOPS (~14 m). Equation 2 implies that a higher Doppler frequency separation results in increased precision of the along-track displacement measurement.

From Equation 1, the Doppler centroid difference Δf_{DC} is positively proportional to T_{diff}; larger time difference between acquisitions in the overlap regions results in greater spectral separation. Assuming constant range distance and azimuth line time, corresponding to the center of the bursts, the timing difference between adjacent burst overlaps in the along-track direction is ~2.76 s. For subswath overlaps in the range direction, which we will refer to as forward subswath overlaps, the time difference between acquisitions is ~0.96 s. In contrast, subswath overlaps in the opposite range direction, which we will refer to as backward subswath overlaps, have a time difference of ~−1.80 s. Consequently, the precision obtained from forward subswath overlaps (SBOI$_{fwr}$) is approximately three times lower than that from burst overlaps, while the precision obtained from backward subswath overlaps (SBOI$_{bwr}$) is about two-thirds of that from burst overlaps (Table 1 and Figure 1).

The spectral separation, however, is not uniform across the overlap regions, as it varies pixel-by-pixel due to three key parameters. First, the antenna beam steering rate (k_ψ) of S-1 TOPS varies across different subswaths, leading to spectral separation differences among subswaths. Second, the range distance (R_0) is not uniform during acquisition, even within the same subswath, as it varies from near range to far range. This variation causes spectral differences in the range direction for overlaps within each individual subswath, particularly for burst overlaps, which have an extent of ∼80 km in the range direction. Finally, the timing difference, T_{diff}, is not consistent along the azimuth direction. This inconsistency results in variations in spectral separation at the pixel level along the azimuth direction, especially for subswath overlaps, which extend in the azimuth direction (∼18 km). These parameter variations necessitate calculating the Doppler spectral separation on a pixel-by-pixel basis along both the range and azimuth directions within the overlap regions to accurately determine the corresponding along-track displacement using Equation 2.

Table 2
LiCS Frame Track IDs and Image Pairs

LiCS track ID	Image pair
014A_05232_242525	20230128–20230305
116A_05207_252525	20230123–20230228
021D_05266_252525	20230105–20230306
123D_05292_242525	20230124–20230301

After calculating the pixel-based scaling factors, we generated the Subswath and Burst Overlap Interferogram (SBOI) for the Kahramanmaraş Earthquakes using two ascending frames (014A, 116A) and two descending frames (021D, 123D) to cover the coseismic displacement field (Figure 2). We selected the most coherent pairs before and after the earthquake, rather than the nearest pairs, due to snowfall following the earthquake, which caused low coherence in the nearest pairs (Table 2). To identify the best coherence pairs for each frame, we examined the coherence matrix by comparing all possible pairs within 6 months before and after the earthquake. The analysis revealed that coherence improved notably in the first week of March as the snow melted, particularly in the northern part of the deformation zone, where snowfall had the greatest impact. In contrast, the southern part of the far field was less affected by snowfall. Notably, in the near deformation zone, the primary coherence drop was clearly caused by the earthquake deformation itself, even though snowfall also contributed (Figures S2 and S3 in Supporting Information S1). To mitigate the effects of decorrelation caused by both snowfall and deformation, we applied adaptive filtering to the SBOIs, which helps to increase Signal-to-Noise Ratio (SNR) of SBOI (Wegmüller et al., 2016).

The varying sensitivity of SBOI in different overlap types is clearly visible near the fault (highlighted as Case 1, 2, and 3 in Figure 3c). For example, the BOI starts wrapping one step earlier than SOI_{bwr}, which means the deformation zone near the second burst overlap (Case 1) exceeds around 0.7 m $(-\pi, \pi)$ of displacement but has not yet reached 1.2 m. The deformation zone near the third burst overlap (Case 2) shows SOI_{bwr} also starts wrapping but SOI_{fwr} has not yet responded. Thus, we can infer that the displacement in this region is higher than 1.2 m but has not yet reached 2.3 m. Finally, in the deformation zone exactly at the rupture location (Case 3), near the fourth burst overlap, SOI_{fwr} starts wrapping; therefore, we can conclude that the displacement in this region exceeds around 2.3 m.

This wrapping phenomenon in the near-field deformation necessitates unwrapping the SBOI to estimate the total displacement. While SBOI mitigates some of the challenges encountered in conventional unwrapping, such as atmospheric delays and strong phase gradients, due to its double-difference nature (Grandin et al., 2016), it introduces a different difficulty: the sparse and discontinuous spatial distribution of the data. SBOIs are only valid within narrow (∼1.5 km) overlap regions, separated by wide (∼17 km) non-overlapping gaps. These large spatial discontinuities violate the connectivity constraints required for conventional two-dimensional unwrapping algorithms such as SNAPHU (Chen & Zebker, 2001), resulting in poor phase continuity and unreliable outputs. Interpolation-based approaches to fill these gaps before unwrapping are highly error-prone especially in complex rupture zones leading to unphysical phase artifacts and loss of deformation detail. A burst-by-burst unwrapping strategy could be considered, but it introduces the additional challenge of referencing each individually unwrapped burst to a common phase baseline. Furthermore, different overlap types (e.g., burst vs. subswath) exhibit distinct phase sensitivities, meaning that a unified unwrapping solution must account for varying resolution ambiguities.

To address these challenges, we implemented a hybrid unwrapping approach that uses azimuth offset tracking (AOT) as a deformation prior (Nergizci et al., 2025). In this method, a variable-median filtered AOT displacement field is converted to a synthetic phase map using pixel-based scaling factors. We then calculate the residual wrapped phase between the observed SBOI and the AOT-derived phase and reconstruct the unwrapped phase by adding this residual back to the synthetic model. This approach preserves fine-scale interferometric details while resolving phase ambiguities without requiring spatial continuity across the frame. For full details of the

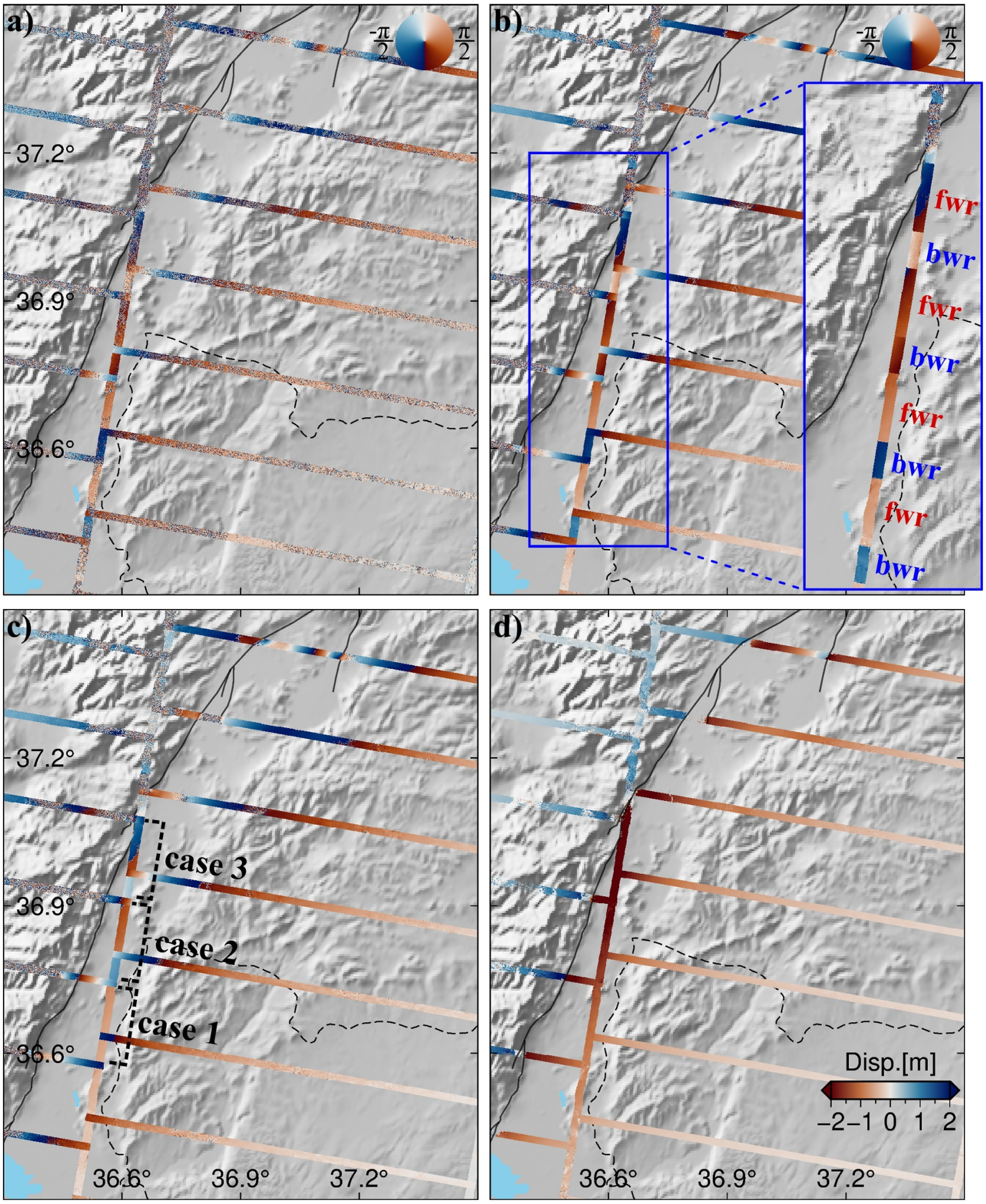

Figure 3. Steps for SBOI generation. (a) Unfiltered wrapped SBOI phase. (b) Filtered wrapped SBOI phase with a zoomed window highlighting the backward and forward subswath near-field deformation. (c) Scaled wrapped SBOI displacement. (d) Unwrapped SBOI displacement. Red indicates deformation in the northern direction, while blue represents deformation toward the south.

methodology and validation using near-fault displacement profiles, see Text S1 and Figures S4, S5 in Supporting Information S1.

Following the phase unwrapping process, we generated SBOI maps for two ascending tracks (014A, 116A) and two descending tracks (021D, 123D) (Figure 4). To validate the SBOI data set, we utilized a GNSS data set comprising 55 stations (20 permanent and 35 campaign) from Özkan et al. (2023). Among these, 20 GNSS points for the ascending frames and 14 for the descending frames were selected, as they are located within or near the burst overlap regions. For comparison, the SBOI signal at each GNSS location was estimated by averaging pixel

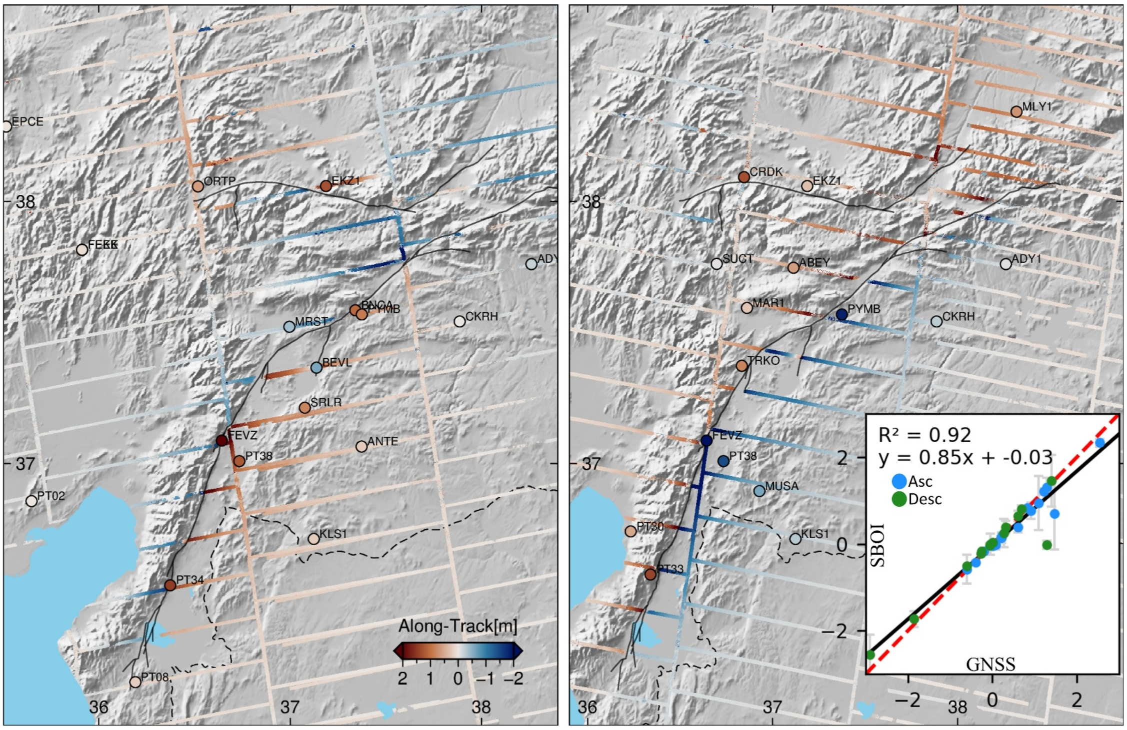

Figure 4. Comparison of along-track displacements from SBOI and GNSS (Özkan et al., 2023). Left and right panels show unwrapped SBOI displacements for ascending and descending tracks, respectively. GNSS horizontal displacements are projected onto the satellite azimuth direction using the respective acquisition heading angles (approximately −10° for ascending and −170° for descending), and are shown as colored circles for direct comparison. Red indicates along-track displacement in the satellite flight direction corresponding to northward motion for ascending tracks and southward motion for descending tracks. The inset shows a linear regression analysis comparing SBOI and GNSS along-track displacements: blue dots represent ascending, and green dots represent descending GNSS projections with the gray errorbars. The red dashed line indicates the one-to-one correspondence, while the black line shows the fitted regression line across all GNSS points.

values within a variable-sized search window (ranging from 5 × 5 to 20 × 20 pixels), depending on the data availability around each point. The horizontal GNSS velocities were projected onto the satellite along-track directions by applying heading angles of −10° for the ascending tracks and −170° for the descending tracks.

Linear regression analysis between the SBOI data set and the GNSS along-track projections (Figure 4) shows a strong correlation, with a regression slope of 0.85 and a coefficient of determination $\left(R^2\right)$ of 0.92. The mean bias between the data sets is modest (−0.03 m), indicating no major systematic error. When analyzing each geometry separately (Figure S6 in Supporting Information S1), we note that for the ascending tracks, station PT34 deviates noticeably from the one-to-one line. This is likely because the station is located approximately 200 m from the rupture segment, where the averaging window may encompass pixels from both sides of the fault, thereby underestimating the displacement. For the descending tracks, most stations align well with the regression line. The primary outlier is station CRDK, likely caused by decorrelation noise or residual unwrapping error in that region.

The consistency between SBOI and GNSS confirms the reliability of overlap interferometry in capturing near-field along-track displacements. Building on this validation, we now explore the spatial deformation patterns resolved by SBOI, including both distributed and localized features along the fault.

Since SBOIs show displacements in the along-track direction, northward displacements in ascending tracks have the opposite sign to those in descending tracks, and vice versa. For visualization, we inverted the sign of the descending track data to represent all northward displacements as red and southward displacements as blue (Figure 5). On the EAF, the deformation in the along-track direction aligns well between the ascending and descending tracks. This indicates that the deformation along the EAF is dominated by north-south displacements. On the second rupture along the ÇSF, discrepancies in color patterns or even opposite signs in the ascending and descending tracks reveal deformation dominated by east–west displacements, associated with strike-slip motion.

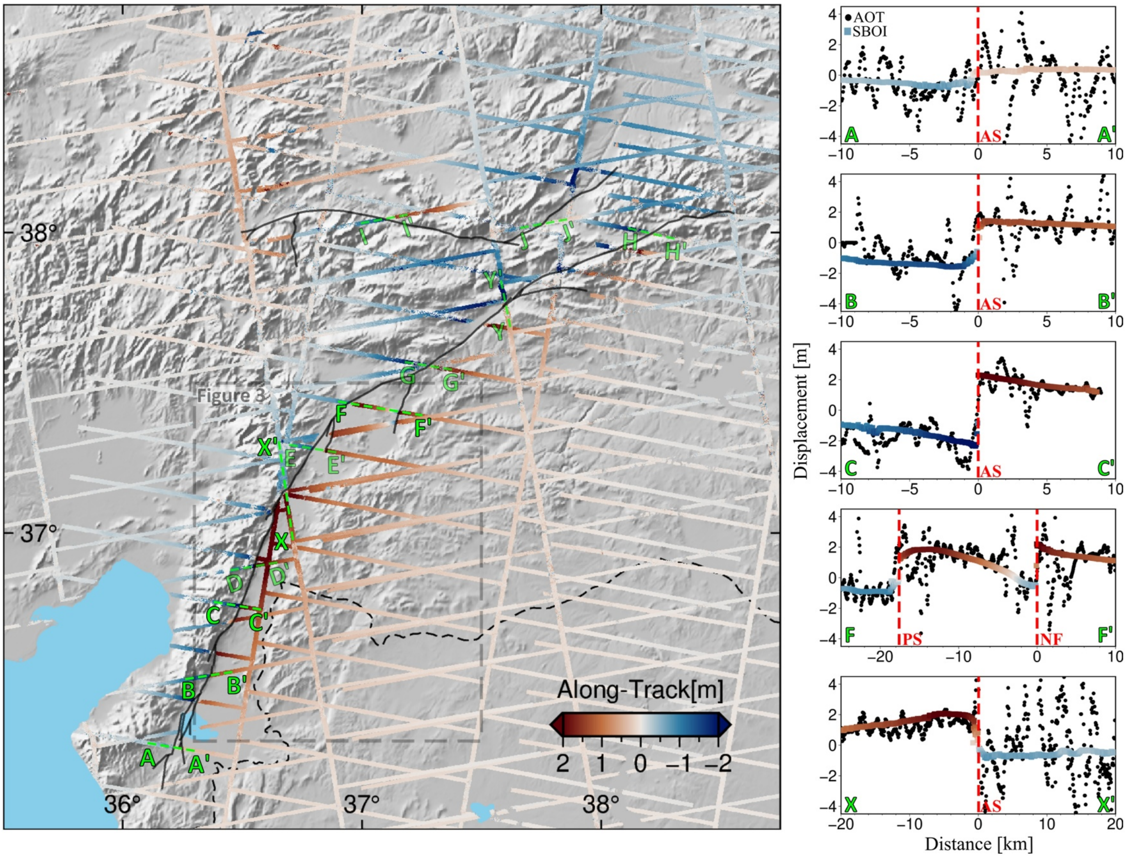

Figure 5. SBOI along-track displacement and example profiles. (Left) Map of unwrapped SBOI from four tracks (021D, 123D, 116A, 014A), with red and blue indicating northward and southward displacements, respectively. Five solid dashed green lines indicate selected profiles (A, B, C, F, and X) used to sample variations in deformation and sensitivity across overlap types. Additional semi-transparent profiles are shown for context and are detailed further in Figure 13. (Right) Along-track displacement profiles from SBOI (colored rectangles) and azimuth offset tracking (AOT, black dots), both shown as median-binned using a 100 m window. Red dashed lines mark mapped rupture traces (AS = Amanos Segment, PS = Pazarcık Segment, NF = Narlı Fault).

The SBOI profiles capture both distributed and localized deformation: for example, displacement localizes near the fault to around 4 m at Profile C, while southwest of the fault, they decrease gradually to below 1 m at Profile A. Notably, despite their lower sensitivity, subswath overlaps at Profile X still capture near-field deformation with a clear pattern. The main sources of uncertainty in the SBOI arise from low coherence due to decorrelation caused by the deformation signal, snowfall, or other factors as well as potential unwrapping errors. Comparison with azimuth offset tracking highlights the higher noise level of AOT, even after applying 100 m median binning for the profiles (Figure 5). Detailed profiles along the rupture zone and their varying patterns are discussed further in Section 4.3.

2.2. Pixel Offset Tracking Method

The short wavelength of Sentinel-1 C-band (~5.6 cm) makes phase unwrapping for coseismic interferograms of large earthquakes particularly challenging. Its high sensitivity to small deformations makes it difficult to obtain reliable phase information in near-field regions where the deformation gradient is extremely high, resulting in decorrelated pixels that cannot be unwrapped. The pixel offset tracking (POT) method is often used to estimate deformation directly in the range and azimuth directions or as a priori input for unwrapping tools to guide or mitigate high phase gradients (K. Jiang et al., 2024; Yun et al., 2007). This is because POT relies on amplitude information rather than the phase component, eliminating the need for a phase unwrapping step and making it unaffected by decorrelated phase issues (Fialko et al., 2001; Funning et al., 2005; Michel et al., 1999). The accuracy of POT techniques depends on the pixel size and is typically 1/30th of the pixel size (Merryman &

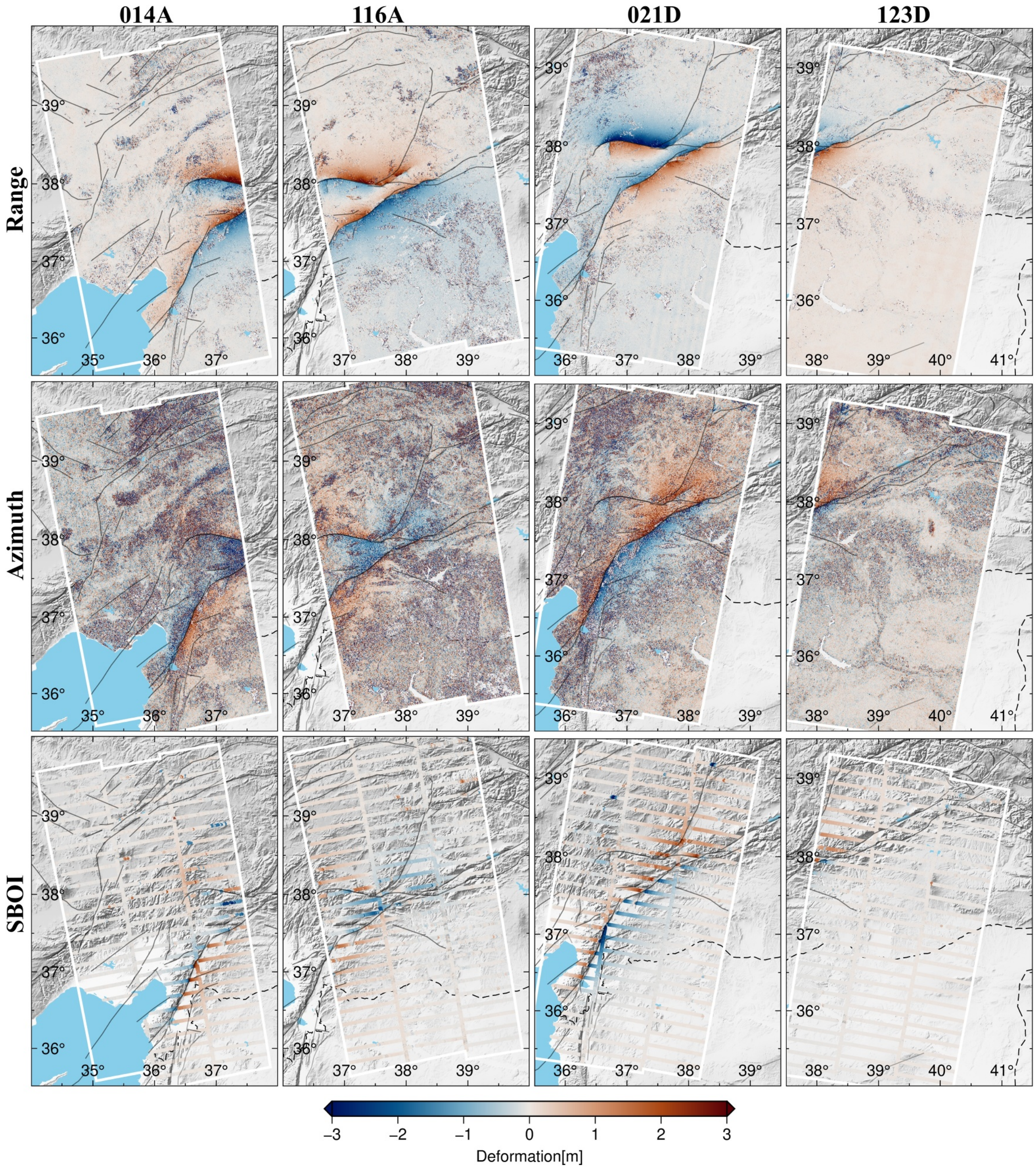

Figure 6. Kahramanmaraş Earthquakes S-1 TOPS data set. (Top) Range offset tracking data sets. (Middle) Azimuth offset tracking data sets. (Bottom) SBOI data sets for tracks 014A, 116A, 021D, and 123D, respectively.

Peter, 2019). Consequently, the POT accuracy is inherently lower by at least one order of magnitude compared to interferometric methods.

For the Kahramanmaraş Earthquakes, we produced range and azimuth pixel offset tracking results of S-1 from ascending frames (014A, 116A) and descending frames (021D, 123D) as input data for both generating 3D displacement fields and performing the slip inversion (Figure 6). Standard S-1 interferograms were not used for this event because the near-field deformation was not fully captured due to the decorrelation caused by the high displacement gradients. While methods such as combining near-field range offsets with far-field InSAR data or guiding range offsets can address this issue, these approaches are beyond the scope of this paper, which focuses on along-track deformation investigation using SBOI.

To compute the pixel offsets, we searched for azimuth and range offsets using 128 × 128 and 64 × 64 pixel windows, spaced by 40 and 16 pixels, respectively, in oversampled, previously deramped mosaics of S-1 TOPS data. The pixel size of the S-1 data is 2.33 m in the range and 13.99 m in the azimuth direction, which results in higher noise levels in the azimuth offset measurements. Offsets with a normalized cross-correlation coefficient greater than 0.1 were selected for further analysis. No filtering was applied to preserve the data set's natural noise ratio, ensuring appropriate weighting during the calculation of the 3D displacement field and the slip inversion process.

2.3. 3-D Displacement Field

Range offset observations are, by definition, measured in the LoS direction, while azimuth offset observations correspond to the along-track direction. Points observed from at least three different acquisition geometries—such as two range offsets (one ascending and one descending) and one azimuth offset—can be decomposed into east, north, and vertical displacement components as follows:

$$\begin{pmatrix} \Delta d_{\mathrm{range},1} \\ \Delta d_{\mathrm{azi},1} \\ \Delta d_{\mathrm{range},2} \\ \Delta d_{\mathrm{azi},2} \\ \vdots \\ \Delta d_{\mathrm{range},n} \\ \Delta d_{\mathrm{azi},n} \end{pmatrix} = \begin{pmatrix} \cos\alpha_1 \sin\theta_1 & \sin\alpha_1 \sin\theta_1 & -\cos\theta_1 \\ -\sin\alpha_1 & \cos\alpha_1 & 0 \\ \cos\alpha_2 \sin\theta_2 & \sin\alpha_2 \sin\theta_2 & -\cos\theta_2 \\ -\sin\alpha_2 & \cos\alpha_2 & 0 \\ \vdots & \vdots & \vdots \\ \cos\alpha_n \sin\theta_n & \sin\alpha_n \sin\theta_n & -\cos\theta_n \\ -\sin\alpha_n & \cos\alpha_n & 0 \end{pmatrix} \begin{pmatrix} \Delta E \\ \Delta N \\ \Delta U \end{pmatrix} \tag{3}$$

where θ represents the local incidence angle, and α is the heading angle, defined as the angle between north and the ground projection of the along-track direction. Like azimuth offsets, SBOIs provide displacement measurements in the along-track direction. This means that SBOIs are not sensitive to vertical movement. The relationship between the along-track displacement (Δd_{azi}) and the horizontal components (ΔE and ΔN) is determined by the heading angle (α) of S-1, which is approximately $-10°$ for ascending tracks and $-170°$ for descending tracks. Therefore, the coefficient for the east component (ΔE) is around 0.17, and for the north component (ΔN), it is approximately 0.98. Consequently, SBOI observations are highly correlated with the north component and but still have some limited sensitivity to the east component.

To decompose the coseismic deformation of the Kahramanmaraş Earthquakes into east, north, and vertical components from S-1 data sets, we applied a weighted least squares (WLS) approach to solve Equation 3. Before performing the decomposition, we corrected for long-wavelength errors in each data set. A planar ramp was estimated from the far-field region excluding the deformation zone and removed separately for each data set (Bagnardi & Hooper, 2018). This step helps mitigate errors introduced by non-tectonic effects such as atmospheric delays, solid Earth tides, and orbital inaccuracies (Lemrabet et al., 2023; Ou et al., 2022). Note that ramp fitting is more challenging for offset tracking data due to its higher noise level, which limits the ability to robustly capture long-wavelength trends (Figure S7 in Supporting Information S1).

In the overlap regions, we used SBOI data due to its superior accuracy compared to azimuth offset measurements. To avoid the influence of noise inherent in azimuth offsets, these measurements were excluded from the overlap regions and used only outside these areas where double-difference interferograms were unavailable. This approach also serves to validate the contribution of the SBOI data set to the calculation of the 3D displacement field.

The decomposition was performed by inverting Equation 3 using the WLS approach. To be included in the inversion, points were required to have at least three different observations. The weights for the WLS were determined by calculating the inverse of the data set uncertainties using a block median approach (Figure S8 in Supporting Information S1). Specifically, the absolute deviation of displacement values from their local mean was computed within predefined pixel windows (e.g., 10 × 10).

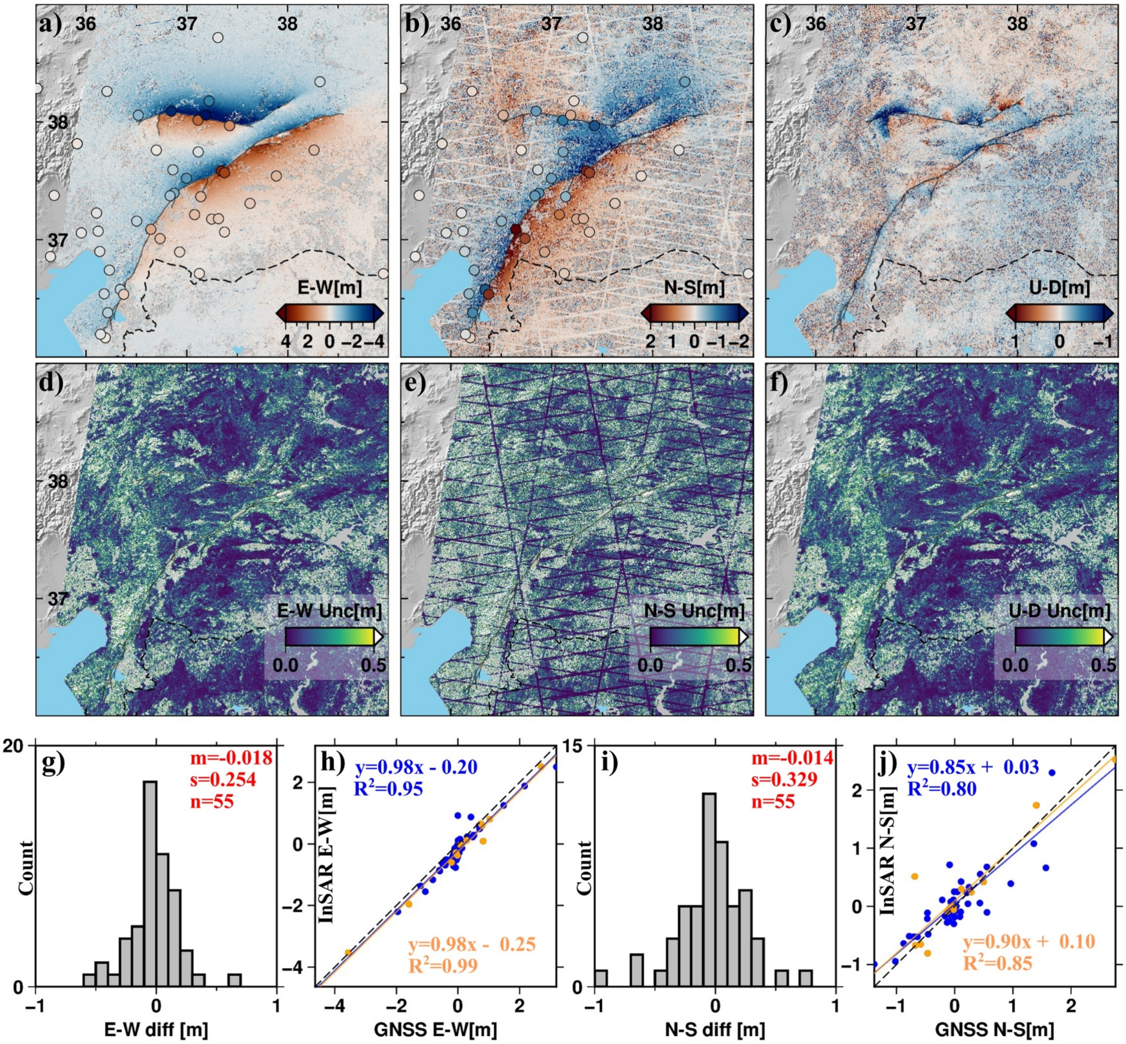

Figure 7. 3-D Displacement Field. (a, d) East-West displacement and its uncertainty. (b, e) North-South displacement and its uncertainty. The circles represent the GNSS data set from Özkan et al. (2023). (c, f) Up-Down displacement and its uncertainty. (g, i) Histograms of the differences between GNSS and S-1 solutions for the east-west and north-south components, respectively. Here, m represents the mean, s is the standard deviation, and n is the number of points of GNSS. (h, j) Linear regression analysis between the S-1 solution and GNSS for the east-west and north-south components, respectively. The orange and blue dots represent GNSS values inside and outside of the SBOI overlap areas, respectively, with GNSS values on the *x*-axis and S-1 values on the *y*-axis. The dashed black line indicates the one-to-one correspondence, while the blue line represents the fitted regression line for all GNSS points, and the orange line represents the fitted regression line for the GNSS points within the overlap regions.

To validate our 3D displacement field, we utilize the 2D GNSS data set (Özkan et al., 2023). Vertical displacement data from GNSS is not available, as their magnitudes are typically 10–40 times smaller than the horizontal displacement, with uncertainty approximately five times higher due to higher noise levels (Özkan et al., 2023). Consequently, our results are not compared with GNSS data for the vertical component (Figure 7).

For the east-west displacement, a pairwise linear regression comparison between the S-1 solution and GNSS observations reveals a strong linear relationship, with a regression gradient of 0.98 and a coefficient of determination R^2 of 0.95. The high R^2 value indicates that 95% of the variance in the GNSS east displacement is explained by the S-1 solution, highlighting strong agreement between GNSS and S-1 solution. Regarding north-south displacement, the comparison shows a slightly weaker relationship, with a regression gradient of 0.85 and a coefficient of determination R^2 of 0.80. While the agreement is somewhat lower than that of the east-west component, the results still indicate a relatively high level of consistency between the S-1 solution and GNSS observations for the north-south component (Figures 7h and 7j). The residuals between GNSS and S-1 for the east component across 55 GNSS points have a mean value of −0.018 m and standard deviation of 0.254 m (1-sigma), while for the north component, the residuals have a mean value of −0.014 m and standard deviation of 0.329 m (Figures 7g and 7i).

In addition, we tested the regression comparison using S-1 results with GNSS points that are within the SBOI data set, specifically those located at least two pixels inside the overlap regions (13 GNSS points). The results show that for the east–west displacement, the coefficient of determination R^2 increased to 0.99, and for the north–south displacement, R^2 increased to 0.85, with a regression gradient of 0.90. These values, being closer to the one-to-one line, indicate a stronger relationship between the horizontal components of the 3-D displacement and the GNSS data set within the SBOI.

The total horizontal displacement was calculated by combining the eastward and northward displacement components using their squared sums. Data points with uncertainties greater than 1 m were excluded to ensure reliable results. To quantify the total displacement along fault ruptures, horizontal displacement maps derived from the decomposed eastward and northward components were analyzed. Displacement values were extracted at 100-m intervals along the rupture trace, with measurements averaged within windows (100 × 100 m) extending 2 km to either side of the fault. The total horizontal displacement was calculated as the difference of displacements on both sides of the fault. The associated uncertainty was computed as the square root of the sum of squared uncertainties from the two sides.

The total displacement profiles along the EAF indicate that the maximum displacement occurred at the center of the Pazarcık segment, where the Narlı Fault intersects with the central part of the Erkenek segment. For the Pazarcık segment, the maximum slip reached 7.8 ± 1.1 m (1-sigma), with a mean displacement of 4.8 ± 1.2 m. Similarly, the Erkenek segment exhibits a maximum slip of 7.9 ± 1.9 m and a mean slip of 4.9 ± 1.3 m. In contrast, the Amanos segment recorded the lowest displacement, with a maximum slip of 4.9 ± 1.3 m and a mean displacement of 3.0 ± 0.8 m.

Our displacement observations along the EAF are consistent with previous studies in the literature (Figures 8c and 8d). The displacement trends align well with the total displacement observations derived from pixel offset tracking of Sentinel-2 data by Provost et al. (2024). Their total offset results, obtained using the arctangent model (Savage & Burford, 1973), fall within our uncertainty range, except at the segment junction between the Pazarcık and Erkenek segments, where their model appears to overestimate the displacement compared to both our results and field studies reported by Karabacak et al. (2023), Meng et al. (2024).

Although the displacement results in the Amanos segment generally agree with those from Provost et al. (2024), their estimates also appear to be greater than our findings. This discrepancy may be attributed to diffuse deformation in the southwestern part of the segment, where the slip zone could extend 5–10 km. However, in our analysis, the total offset displacement was constrained within a 2 km buffer on either side of the fault, which may explain the observed differences.

Field observations (Karabacak et al., 2023; Meng et al., 2024) and high-resolution optical imagery (0.3–0.8 m) (P. Liang et al., 2024) also largely fall within our uncertainty range. However, field observations in the Erkenek segment are notably sparse compared to the Amanos and Pazarcık segments, primarily due to heavy snowfall, which hindered access and limited direct measurements, particularly in the central portion of the segment.

Regarding the ÇSF, the Çardak Fault, where the Mw 7.6 earthquake nucleated, exhibited the highest displacement, with a maximum value of 8.8 ± 0.5 m and a mean displacement of 7.0 ± 0.8 m. Interestingly, the rupture magnitude did not significantly decrease at the segment junction in the west, continuing into the Savrun Fault with a mean slip of 4.8 ± 1.6 m. This rupture behavior has been explained in the literature as a result of supershear rupture propagation, as agreed upon by several studies (Jia et al., 2023; C. Liu et al., 2023; Melgar et al., 2023; Ren et al., 2024; Zhang et al., 2023). On the eastern side of the rupture, displacement values gradually decrease, tapering off toward the end of the Doğanşehir segment. Our displacement results for the ÇSF are consistent with those derived from Sentinel-2 data; however, ground truth validation is limited due to insufficient field observations and high-resolution imagery. This is primarily due to adverse conditions such as heavy snowfall, dense vegetation, and persistent cloud cover, which have hindered efforts to obtain detailed ground-based measurements (Karabacak et al., 2023; P. Liang et al., 2024).

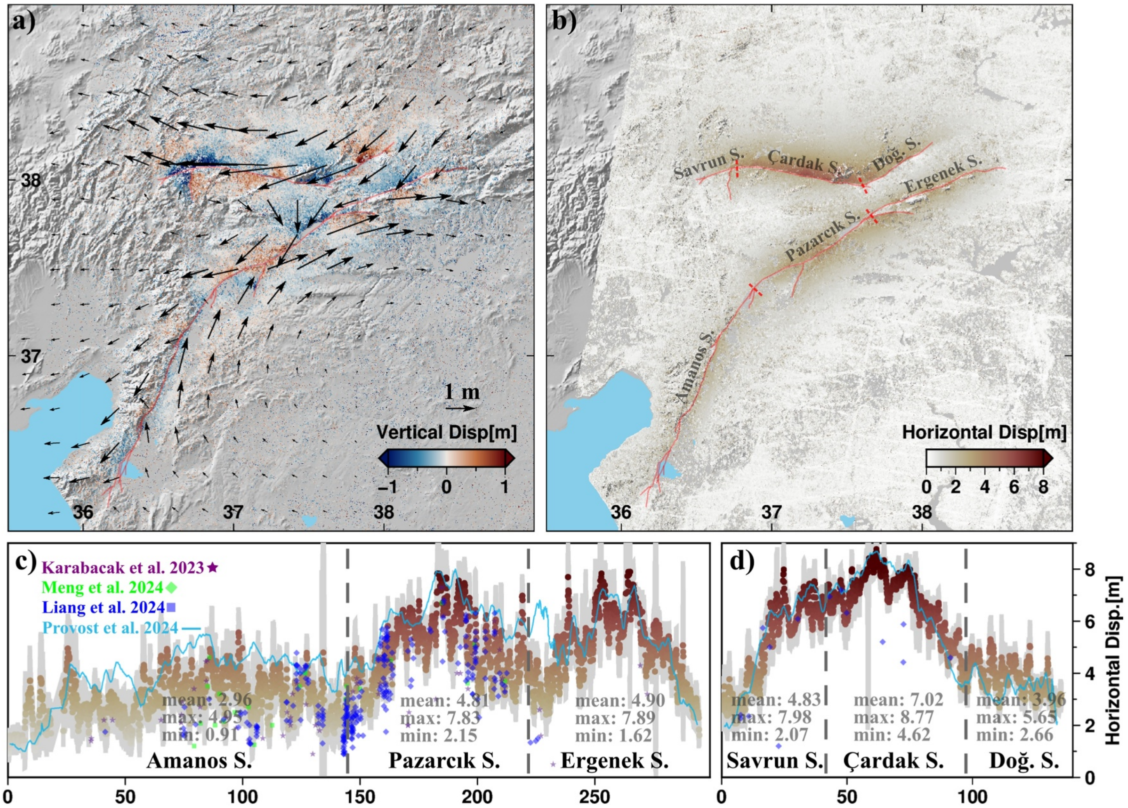

Figure 8. 3D Displacement Map. (a) Vertical displacement with vectors representing horizontal displacements. The color bar indicates subsidence in blue and uplift in red. (b) Horizontal displacement, where the red line represents the fault rupture, and the dashed perpendicular red lines mark segment boundaries along the fault rupture. (c, d) Total displacement derived from horizontal displacement along the fault rupture for the EAF and ÇSF, respectively. The gray shading represents the uncertainty at the 95% confidence interval for displacement. The purple stars represent field observations from Karabacak et al. (2023), the green diamonds correspond to field observations from Meng et al. (2024), and the blue rectangles indicate high-resolution optical image observations from P. Liang et al. (2024). The blue lines represent the total displacement of the fault rupture derived from Sentinel-2 data by Provost et al. (2024).

3. Coseismic Slip Inversion

3.1. Fault Segment and Geometry Setup

We defined 10 planar fault segments to characterize the fault geometries; six for the EAF and four for the ÇSF, representing the total rupture from the two earthquakes (Figure 9). We subdivided Amanos and Pazarcik segment into two smaller segments to better capture the variation in strike angles that could not be accurately represented with a single large segment, while the other segments were considered well represented as single large segments. The preliminary strike angles of the segments were estimated from the range offset data set and the surface rupture map provided by the USGS service (USGS, 2023).

For the estimation of specific strike and dip angles, we employed the Geodetic Bayesian Inversion Software (GBIS) (Bagnardi & Hooper, 2018). The strike angle was constrained to ±5° around the preliminary estimates, while the dip angle was left unconstrained. After determining the strike and dip angles for each segment, we defined variable patch sizes to account for the decreasing fault resolution with depth (Fang et al., 2022; Lohman & Simons, 2005). Patch sizes were approximately ∼2 km at the top, increasing to ∼4 km at depths of 2–6 km, ∼6 km at depths of 6–12 km, and ∼8 km in the final layer at depths of 12–20 km (Figures S9 and S10 in Supporting Information S1).

3.2. Geodetic Bayesian Slip Inversion

We performed the inversion of offset tracking and SBOI data sets using a Bayesian approach, employing a Markov Chain Monte Carlo (MCMC) method based on the Metropolis-Hastings algorithm (Bagnardi & Hooper, 2018). This methodology, implemented as an updated version of the GBIS, systematically samples the

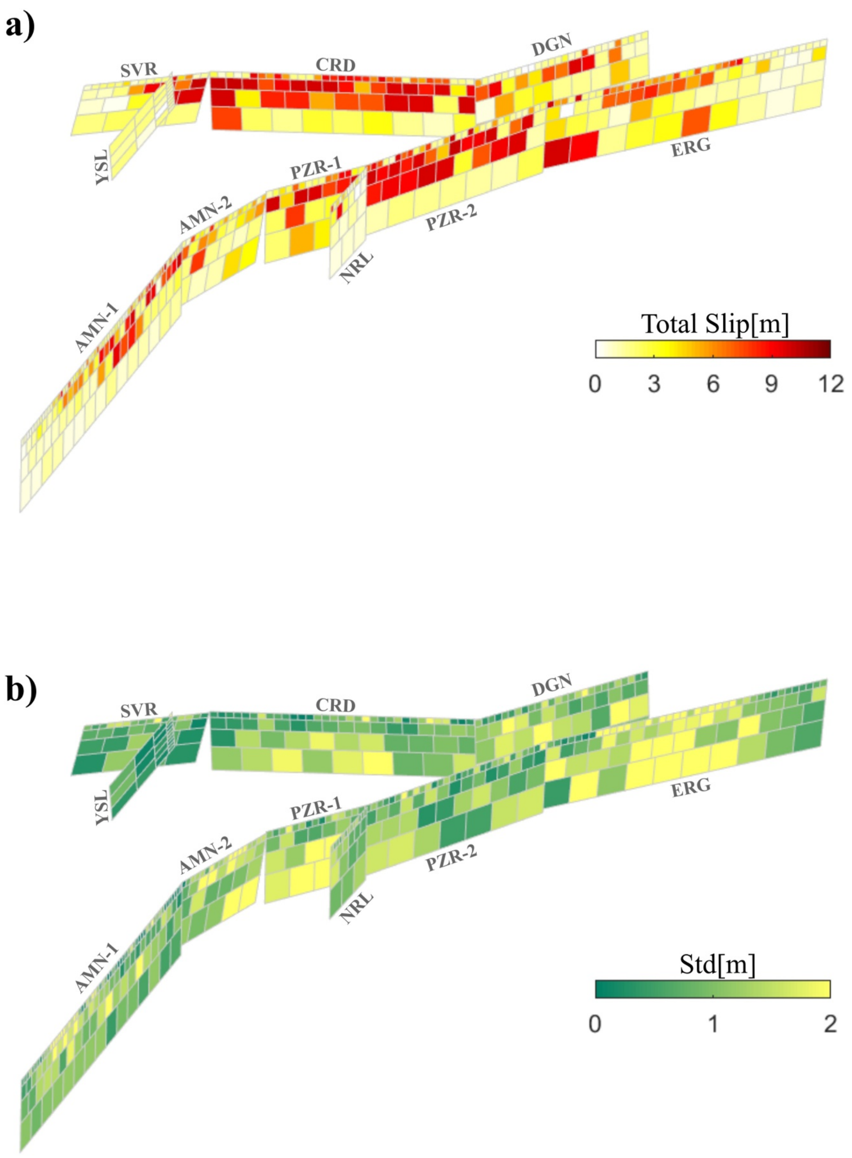

Figure 9. Coseismic Total-Slip Distribution of the Kahramanmaraş Earthquakes derived from range, azimuth offset, and SBOI data sets. (a) Total slip distribution, calculated as the square root of the sum of squared median slip components (strike-slip and dip-slip) for each patch. The strike-slip and dip-slip values were derived from the median of the posterior samples in the Bayesian inversion. (b) Uncertainty of the slip patches, calculated as the square root of the sum of squared standard deviations of the strike-slip and dip-slip components for each patch. These values were computed from the PDFs of the GBIS inversion, reflecting both observational noise and modeling uncertainties.

posterior Probability Density Function (PDF) of each model parameter to estimate the slip distribution on individual fault patches. The method facilitates a comprehensive exploration of the parameter space while incorporating data uncertainties and prior information. Notably, our approach avoids the use of spatial smoothing techniques, such as Laplacian or von Karman regularization, ensuring that the solution reflects the data constraints without imposed regularization.

To prepare for the inversion, we calculated the semi-variogram of each data set over non-deforming regions to estimate the spatial error covariance (Bagnardi & Hooper, 2018). Given the differing noise levels among the three data sets, proper weighting is crucial to achieving reliable inversion results. This step is essential for constructing the covariance matrix of each data set, which determine their respective weights and influence on the inversion process (Figure S11 in Supporting Information S1).

Afterward, we downsampled the offset data points using a variable uniform downsampling method, maintaining higher density near the fault and progressively sparser spacing farther from the fault. Specifically, we used a 0.015° interval within 0–10 km of the fault, 0.030° within 10–20 km, 0.055° within 20–50 km, 0.1° within 50–100 km, and 0.2° beyond 100 km. For SBOI, we downsampled the data at 0.010° interval from near field to 50 km and 0.020° interval beyond 50 km the fault (Figure S12 in Supporting Information S1). To address potential ambiguities in segment definitions near the rupture trace, as well as noise and unwrapping errors, we masked out data within 1 km of the fault.

To minimize the influence of large noise inherent in the offset tracking data, we applied a noise reduction step prior to the inversion. This involves setting a threshold between the unfiltered offset tracking and the median-filtered results. Data points were flagged as outliers and removed if the difference between the unfiltered and filtered offsets exceeds 3 m for the azimuth offset or 1.5 m for the range offset (Figures S13 and S14 in Supporting Information S1). The thresholds for azimuth and range offsets were determined through a trial-and-error process to identify the optimal values.

We used rectangular dislocation sources in an elastic half-space (Okada, 1985), assuming a Poisson's ratio of $\nu = 0.25$ and a shear modulus of $\mu = 40$ GPa. For each fault segment, rather than solving for the rake angle, we separately estimated the left-lateral strike slip and dip slip components, setting the strike slip bounds between 0 and 10 m and the dip slip bounds between -2 and 2 m to account for potential minor normal or thrust faulting along the EAF and ÇSF.

3.3. Inversion Results

The slip inversion, incorporating range offset, azimuth offset, and SBOI observations, indicates that the maximum slip occurred in the Pazarcık segment of the EAF and Çardak segment of the ÇSF (Figure 9). The coseismic slip is primarily concentrated in the shallow parts of the faults, extending to depths of approximately 12 km for both events. However, in certain areas of the Erkenek segment and near fault junctions, the slip extends to deeper patches. In the Pazarcık segment, slip is distributed over a broad area, accumulating at the junction with the Narlı Fault, where it reaches a maximum of 11 m at shallow depths. In the Erkenek segment, slip is concentrated in the central portion, with a maximum displacement of 8 m at shallow depths, tapering approximately 15 km northwest of the segment, which aligns with the aftershocks distribution (Figure S15 in Supporting Information S1). The Amanos segment exhibits slip primarily in the central zone, with lower values compared to the Pazarcık segment, and it gradually tapers approximately 40 km southeast of the segment. In the ÇSF, the Çardak segment exhibits a maximum slip of over 11 m, with significant concentration in the upper sections and tapering at depth. The junction between the Çardak and Savrun faults shows considerable slip accumulation, with deformation extending to deeper patches. The Doğanşehir Fault, in contrast, exhibits more subdued rupture behavior, with slip values below 5 m.

Note that the coseismic slip patterns appear spatially discontinuous due to the absence of regularization in the inversion process (Figure 9a). The lack of smoothing results in a patchy slip distribution at shallow depths, which complicates the interpretation of rupture dynamics, particularly the investigation of shallow slip deficits (Fialko et al., 2001; X. Xu et al., 2016). These features may result from the 1-km mask applied to the near field, as well as from noise in the data sets caused by snow cover, unresolved unwrapping errors, or the absence of smoothing constraints in the inversion.

To assess the uncertainty of slip estimates, variability in the posterior distribution of the sampled patches during the MCMC process was analyzed. The standard deviation σ_i for each patch was calculated after removing the burn-in phase, and ensuring convergence (Figure 9b). The analysis reveals that shallow patches, particularly in the central portions of the Pazarcık and Çardak segments, exhibited low uncertainties ($\sigma < 0.5$ m), indicating they are well-constrained by the available data. In contrast, higher uncertainties ($\sigma > 1$ m) are observed in the Erkenek segment and parts of the Amanos segment, affecting both upper and lower patches. These regions of higher uncertainty likely reflect the noisiness of the offset tracking data, potential undetected unwrapping errors in the SBOI data set due to snowfall and high phase gradients, and possible complexities in fault geometry or rupture dynamics.

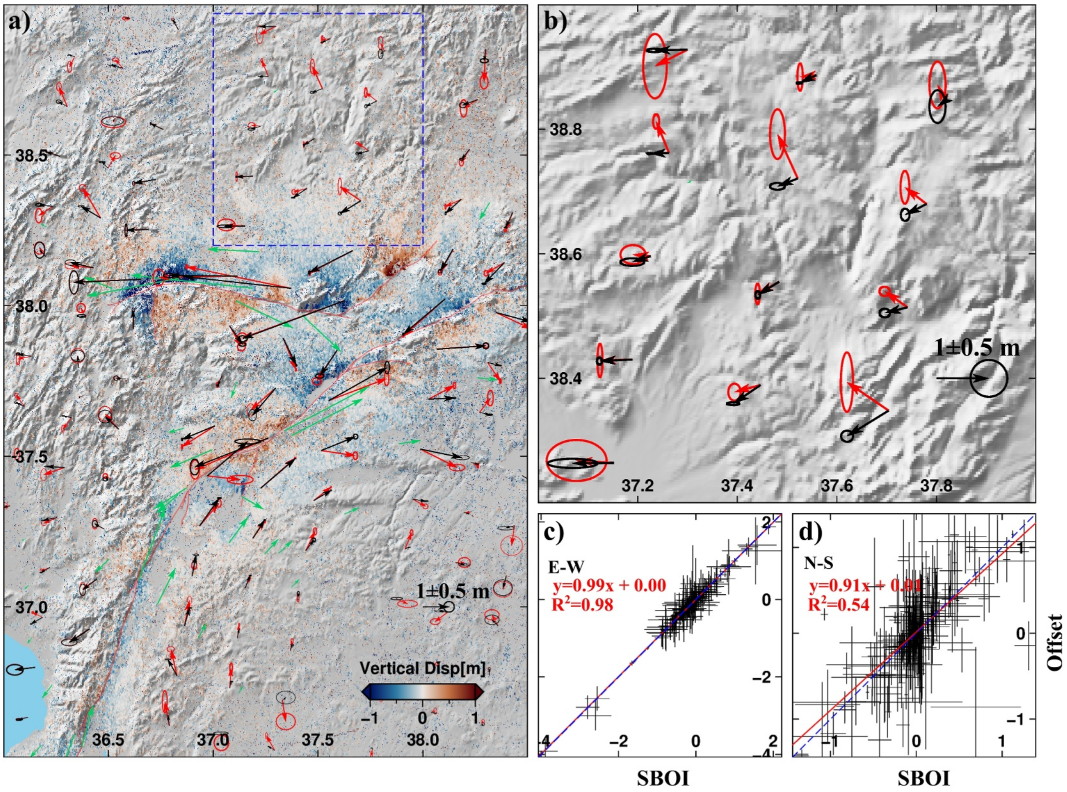

Figure 10. Comparison of 3D displacements with and without the SBOI solution. (a) Comparison of horizontal displacement vectors at 375 points within the overlap regions. Red vectors represent the displacement solution without the SBOI data set (offsets-only solution), black vectors represent the displacement solution with SBOI, and green vectors indicate GNSS horizontal displacement. The colormap represents vertical displacement, with blue indicating subsidence and red indicating uplift. The blue dashed rectangle highlights the zoomed region shown in panel (b). (b) Close-up view of the zoomed region from (a), providing a detailed comparison of displacement vectors. (c, d) Linear regression analysis of horizontal displacement solutions with and without SBOI for the east-west (E–W) and north-south (N–S) components, respectively. The blue dashed line represents the one-to-one line, while the red line indicates the linear regression fit. Crosses represent the displacement values, with the solution with SBOI on the *x*-axis and the solution without SBOI on the *y*-axis, including the uncertainties as error bars.

4. Discussion

4.1. Impact of SBOI on 3D Displacement Field

To assess the impact of SBOI on horizontal displacement, we analyzed 375 sample points within the overlap regions along the ascending tracks (Figure S16 in Supporting Information S1) to compare horizontal displacement results with and without SBOI. For these points, we calculated the mean east and north displacement values, along with their corresponding uncertainties, by averaging neighboring pixel values within a 50 × 50 pixel window, using solutions derived from offset tracking and SBOI (Figure 10). The horizontal displacement vectors illustrate noticeable differences in direction between the solutions with and without SBOI. Notably, the SBOI-based vectors align more closely with GNSS displacement measurements (green vectors) and pre-calculated 2D horizontal vectors at 20 km intervals, underscoring the improved accuracy introduced by the SBOI data set (Figure 10a). A close-up view of a zoomed-in region (Figure 10b) reveals finer-scale variations in displacement vectors and shows that some SBOI vectors deviate from the azimuth offset solution, particularly in the northerly direction, where offset tracking displays larger uncertainty ellipses. The horizontal displacement pattern from SBOI aligns more consistently with the modeled deformation field in Figure 8a.

To further evaluate the effect of SBOI on the 3D displacement field, we conducted a statistical comparison using linear regression and the coefficient of determination (R^2) between solutions derived from offsets alone and those incorporating SBOI (Figures 10c and 10d). For the east-west component, the analysis reveals a regression gradient of 0.99 and an R^2 value of 0.98, indicating near-identical results for both cases. This suggests that the offset data sets alone provides sufficient constraints for the east-west component of the displacement field, and the SBOI data set does not significantly alter this component.

In contrast, the north-south component demonstrates a more substantial effect. The regression analysis shows a gradient of 0.91 and a lower R^2 value of 0.54, indicating that the inclusion of SBOI significantly alters the constraints on the north–south component at these points.

The uncertainties in north-south deformation for the 375 points were reduced with the inclusion of SBOI, as the mean inversion uncertainty decreased from 0.27 m (offsets-only) to 0.12 m (SBOI). For the east-west component, the mean uncertainty decreased from 0.20 m (offsets-only) to 0.18 m (SBOI) (Figure S17 in Supporting Information S1). These results underscore SBOI's critical role in constraining the north-south component of displacement, where range and azimuth offsets alone are insufficient to capture the full deformation field, while also providing slight improvements in the east-west component.

4.2. Impact of SBOI on Coseismic Slip Inversion

To investigate the impact of SBOI on geodetic slip inversion, we carried out the inversion using six different combinations of S-1 data sets: (a) Range offset + Azimuth offset + SBOI (RAS), (b) Range offset + Azimuth offset (RA), (c) Range offset + SBOI (RS), (d) only Range offset (R), (e) only Azimuth offset (A), and (f) only SBOI (S). This approach enables us to focus on how SBOI data impacts inversion outcomes at various depth ranges and influences the stability and accuracy of the results. The same geodetic inversion strategy described in Section 3.2 was consistently applied in all cases.

The inversion results from individual data sets reveal distinct constraints on slip distribution (Figure 11a). Among these, the range offset inversion closely resembles the joint inversion (RAS) as the range offset captures LoS displacement, which integrates contributions from the east, north, and up components. However, its sensitivity to the north component is limited. In contrast, the azimuth offset and SBOI inversions primarily reflect along-track displacement, which is dominated by the north component.

The Amanos segment has a strike angle of approximately 24° in the southwest section, with a dip angle of 85°, characterizing it as a left-lateral strike-slip fault. This fault geometry is nearly parallel to the S-1 descending track, posing significant challenges in observing deformation from the LoS direction (Lu et al., 2025). The range and azimuth solutions indicate that, without incorporating SBOI, slip along this part of the Amanos segment is underestimated and scattered into deeper patches (Figure 11a). This occurs because the range offset alone is insufficient to capture the true deformation in the LoS direction, while the azimuth offset exhibits excessive noise, reducing its reliability in capturing the actual displacement. However, the inclusion of SBOI in the solution helps to better constrain the slip in this segment. A similar challenge is observed for the Doğanşehir segment, which also aligns closely with the S-1 flight direction, highlighting the importance of SBOI in accurately resolving deformation in such geometries.

Notably, each individual solution highlights significant slip in the Pazarcık segment of the EAF and the Savrun and Çardak segments of the ÇSF. While the slip is predominantly concentrated in the shallow parts of these segments, the single solutions also assign slip to deeper patches, reflecting the limitations of individual data sets in fully capturing the deformation field (Figure 11a). The azimuth offset solution exhibits a smoother slip distribution but overestimates slip at depth. This behavior arises from the higher uncertainty in the azimuth offset data set, which leads to underconstrained patches in far-field deformation zones. In comparison, the SBOI solution reveals more scattered patches and irregular spatial patterns, reflecting its sparse coverage restricted to overlap regions.

The dual combinations of slip inversion demonstrate that SBOI significantly enhances the constraints on the inversion, whereas the azimuth offset provides comparatively limited additional constraint. To assess the impact of different data sets, we calculated the differences between the joint inversion and both the dual combinations (RA, RS) and the only range offset solution (R) (Figure 11b). The comparison reveals that the combination of range offset and SBOI (RS) produces results most consistent with the joint inversion, while the inclusion of the azimuth offset (RA) does not significantly alter the solution, closely resembling the only

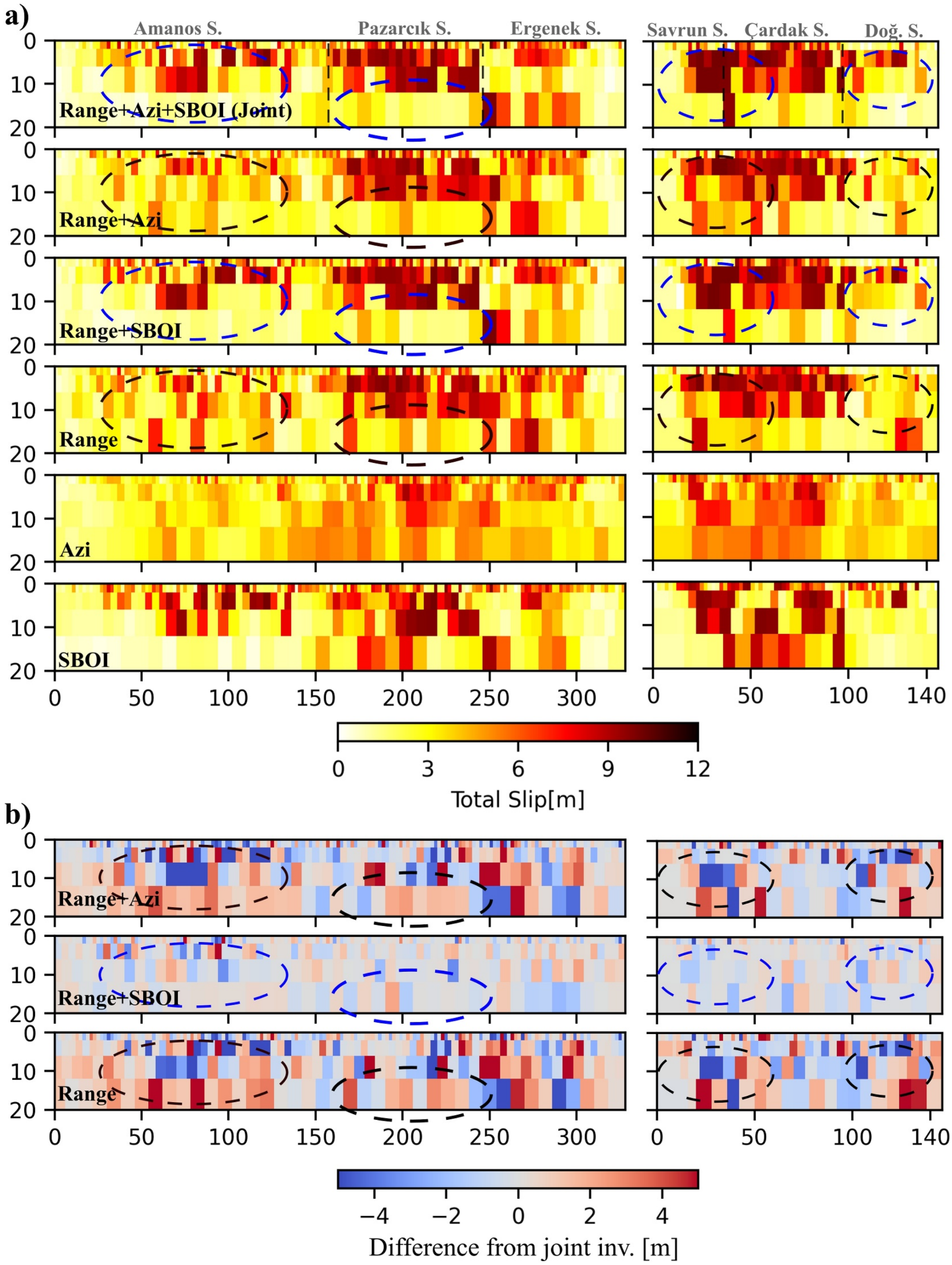

Figure 11. Median slip distribution and differences for various combinations of S-1 data sets (a) Total slip distribution of the fault segments derived from different data set combinations. The colormap represents the total slip in meters. (b) Differences in slip distribution compared to the Range + Azimuth + SBOI (joint) solution for selected combinations (Range + Azimuth, Range + SBOI, and Range only). The colormap represents the magnitude of the difference in meters, where blue indicates underestimation and red indicates overestimation relative to the joint solution. Black and blue ellipses highlight the influence of SBOI on the inversion results.

range offset (R) inversion results. This outcome highlights that the azimuth offset data set lacks the precision required to effectively constrain the slip inversion, showing minimal impact both at shallow depths and in deeper regions.

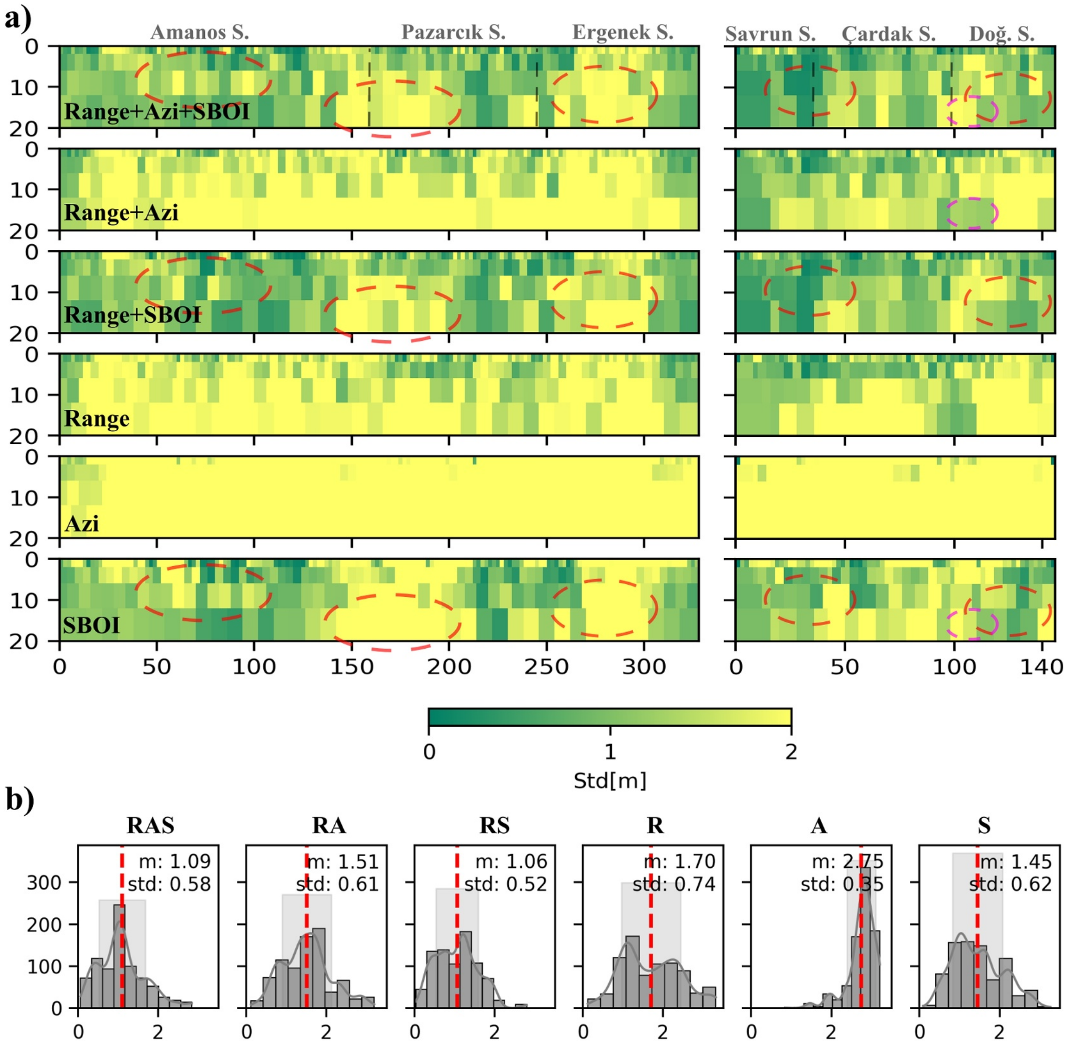

Figure 12. Comparison of slip inversion uncertainties across various combinations of S-1 data sets. (a) Slip uncertainty distribution of the fault segments derived from different data set combinations. The colormap represents the standard deviation of the slip in meters, with lower values indicating better-constrained estimate. Red ellipses highlight the influence of SBOI on the uncertainty results. (b) Histograms of slip uncertainties for all data set combinations. Gray bars represent the frequency of uncertainties, while gray lines show the Kernel Density Estimation (KDE), providing a smoothed approximation of the uncertainty distribution. Red dashed lines indicate the mean, m, and transparent rectangles highlight one standard deviation, std, around the mean, illustrating the spread of uncertainty values for each combination.

To assess the uncertainty of slip estimates for each patch obtained from Bayesian inversion, we analyzed the variability in the sampled posterior distribution during the MCMC process. Figure 12 shows that the combination of range offset and SBOI (RS) achieves the lowest patch uncertainties with a mean uncertainty of 1.06 m. This is closely followed by the joint inversion with a mean uncertainty of 1.09 m. While the inclusion of more redundant data is generally expected to improve the constraints, the noisy nature of the azimuth offset introduces higher solution uncertainty, reducing the reliability of the inversion results.

In particular, the only azimuth offset solution (A) has the highest uncertainties with a mean uncertainty of 2.75 m, which negatively affects the inversion when included in various combinations. The histograms in Figure 12b show the spread of uncertainties for each combination in more detail, highlighting the improved performance of SBOI-based solutions.

Noticeable patterns in the spatial distribution of uncertainties reveal certain areas with significantly higher values. In the central region of the Amanos segment, the joint inversion model incorporating azimuth offset data exhibits greater uncertainties compared to the Range + SBOI solution. A similar trend is observed at the intersection of the Amanos and Pazarcık segments, as well as in the Erkenek segment, as highlighted by red ellipses in Figure 12a. At the Amanos-Pazarcık segment intersection, the SBOI-only data set also shows elevated uncertainties, likely due to fault complexity in this region. Additionally, the proximity of the Narli Fault, where the Mw 7.8 earthquake nucleated, further contributes to the complexity of the deformation field. In the Erkenek segment, higher uncertainties are primarily attributed to signal decorrelation caused by snowfall, along with residual, unidentified unwrapping errors in the region.

The variation in uncertainties along the ÇSF follows a different pattern across different locations. For example, at the junction between the Savrun and Çardak faults, the joint inversion and RS inversion results appear similar. However, at the junction between the Çardak and Doğanşehir faults, the joint inversion exhibits higher uncertainties than the dual-inversion results, and in this case, the inclusion of SBOI further increases the uncertainty. Additionally, along the Doğanşehir fault, the incorporation of azimuth offset data improves the uncertainty in the joint inversion results for that area.

Finally, the residual analysis of modeled SBOIs provides further insights into the impact of SBOI (Figure S21 in Supporting Information S1). The modeled SBOIs from the offset tracking combination reveal that the residuals between the model SBOI and observations exhibit higher uncertainties for both range and azimuth offset results. This indicates that these data sets cannot effectively constrain the SBOI information due to the low sensitivity of range offsets in the north-south direction and the high noise levels in azimuth offsets. In contrast, the joint solution significantly reduces residuals, demonstrating that the SBOI model provides a much better fit to the SBOI observations.

These comparisons emphasize the critical role of SBOI in improving slip inversion results, particularly for faults involving significant north-south displacement. Despite its sparse nature, SBOI provides robust constraints, enhancing both the accuracy and precision of the inversion, especially in regions where range and azimuth offsets alone are insufficient.

4.3. Near Fault Displacement From SBOI

Earthquakes generate permanent deformation, that is, typically concentrated along the main fault plane, forming a narrow zone of high-strain, localized slip. This on-fault deformation is often accompanied by more diffuse, distributed inelastic deformation in the surrounding medium, referred to as off-fault deformation (OFD). Together, these components constitute the broader fault zone (Ben-Zion & Sammis, 2003; Chester & Logan, 1986; Mitchell & Faulkner, 2009). Analyzing both on- and off-fault deformation is essential for understanding fault properties and mechanics, including segmentation, surface roughness, structural maturity, and other key characteristics (Antoine et al., 2021; Milliner et al., 2015; Perrin et al., 2016; Scott et al., 2018). Off-fault deformation also helps constrain the earthquake energy budget and long-term strain accumulation, while widening the zone of potential surface rupture relevant to seismic hazard.

Near-field geodetic observations are crucial for capturing on- and off-fault deformation patterns. However, traditional InSAR often fails in regions of high displacement gradients near faults due to phase aliasing. Alternative SAR/InSAR methods, such as offset tracking or multiple-aperture interferometry, can be used in such cases but typically offer limited spatial resolution (Fialko et al., 2001; Jolivet et al., 2014; J. Liu et al., 2025). In the literature, high-resolution optical imagery is commonly used for near-field observations, as it enables precise measurement of surface displacement in high-strain zones (Antoine et al., 2021; Hayek et al., 2024; C. Li et al., 2023).

While SBOI has lower precision than standard InSAR, its ability to resolve displacements in areas where conventional InSAR becomes decorrelated due to excessive phase gradients makes it particularly valuable for studying near-field deformation along fault ruptures. As mentioned in Section 2.1, SBOI can capture both distributed and localized deformation in the near-field along the Kahramanmaraş earthquakes rupture at the overlap regions. To investigate the deformation characteristics, we selected 12 SBOI profiles across different segments and modeled each profile following the approach of J. Liu et al. (2025), which analyzed the near-field deformation of the Kahramanmaraş earthquakes using 3D displacement fields derived from combined SAR/InSAR observations. Their methodology is notable for employing a physically based elastic dislocation model (Savage & Burford, 1973) to fit the observed displacement in the far field ($|x| > 3$ km), allowing estimation of fault slip and locking depth without assuming constant or linear behavior outside the damage zone (Figure S22 in Supporting Information S1). The difference between this elastic model and the observed near-field displacement ($|x| < 3$ km) is interpreted as absent surface displacement (ASD), reflecting distributed inelastic deformation. These ASD residuals are further modeled with a logarithmic decay function to quantify the spatial extent and intensity of off-fault damage (J. Liu et al., 2025).

The SBOI profiles and modeled off-fault deformation (OFD) zones are shown in Figure 13, alongside the fault zone width derived by J. Liu et al. (2025) and the aftershock distribution from (Lomax, 2023). On the Amanos segment, Profile A (southwestern Amanos segment) lies at the rupture termination. The SBOI data reveal a broadly distributed deformation pattern, with total displacement below 1 m. The extensive aftershock zone and wide damage width support a horsetail-like rupture termination scenario (Pucci et al., 2025).

Profile B, ∼30 km northwest of Profile A, exhibits a peak displacement of 2.5 m and a clearly asymmetric damage pattern, evident in both SBOI and the combined model zone width estimates. This asymmetric pattern cannot be easily explained by differences in surface geology: the narrower deformation zone on the right lies in Quaternary continental deposits, while the broader left-side zone occurs within mechanically stronger Mesozoic ophiolites (MTA, 2025). Alternative explanations include rupture directivity, dynamic stress field asymmetry, or fault roughness effects, as noted in prior studies (Dor et al., 2006; Mitchell & Faulkner, 2009). However, detailed dynamic or structural modeling would be needed to fully investigate these effects.

Profiles C and D, located ∼30 km further northwest past a restraining stepover, exhibit highly localized deformation with displacements exceeding 4 m (Figure 13). SBOI accurately captures the localization, whereas combined model overestimates the fault zone width, particularly in Profile D. This segment of the Amanos Fault is geometrically simpler, lacking splays or bends. Teleseismic and strong-motion studies suggest this segment hosted a localized supershear rupture, beginning after the restraining bend near Profile X and continuing to the releasing bend near Profile B (Wan et al., 2024; Yao & Yang, 2025; Zhang et al., 2023). Although rupture speed alone may not control the extent of OFD, the structural simplicity in this region likely promotes more focused, localized deformation.

Profile X and E, ∼30 km further north, mark the northern Amanos segment as it transitions toward the Pazarcık segment. A slight change in fault strike, combined with increased structural complexity, splays, and stepovers, corresponds to broader and more asymmetrical deformation. The left side of the fault zone shows a particularly wide deformation zone. At Profile E, the fault width increases where the Amanos and Pazarcık segments merge. The region between them displays poor signal quality in SBOI due to decorrelation.

Profile F spans the junction of the Pazarcık and Narlı faults, where the Mw 7.8 earthquake nucleated. The Narlı Fault displays sharp, localized deformation exceeding 3 m. In contrast, the Pazarcık segment exhibits a broad asymmetric deformation zone, ∼5 km wide on the right side. This region is characterized by complex coseismic deformation in a wedge-shaped block between the faults, involving counterclockwise block rotation and compression (Magen, Baer, Ziv, Inbal, Nof, et al., 2024).

Profile G is located on the Pazarcık segment, immediately northwest of its intersection with the Narlı Fault. This profile exhibits a peak displacement exceeding 4 m, accompanied by distributed deformation on both sides of the fault. However, the SBOI signal becomes increasingly noisy in this area, likely due to residual decorrelation effects from snow cover, despite the application of most coherent pair selection.

Profile Y captures the transitional zone where the Pazarcık segment curves into the Erkenek segment. In this bend region, the observed deformation decreases to approximately 1 m, with the strain becoming more broadly distributed. Both the SBOI and combined SAR/InSAR models reflect this pattern consistently, highlighting the influence of geometric complexities and rupture dynamics in modulating near-field deformation.

Profiles H and J, on the Erkenek and Doğanşehir faults respectively, show highly decorrelated SBOI signals, mainly due to persistent snow cover. This limits the reliability of quantitative modeling in these areas. Profile I shows sharp deformation across the Çardak Fault; however, the SBOI signal becomes noisy on the far-right side of the fault, leading to an overestimation of fault zone width in the SBOI model. The combined model further overestimates the width on both sides.

This analysis highlights the complementary role of SBOI in characterizing near-field fault deformation, especially in regions where standard InSAR fails due to phase decorrelation or large displacement gradients. Despite

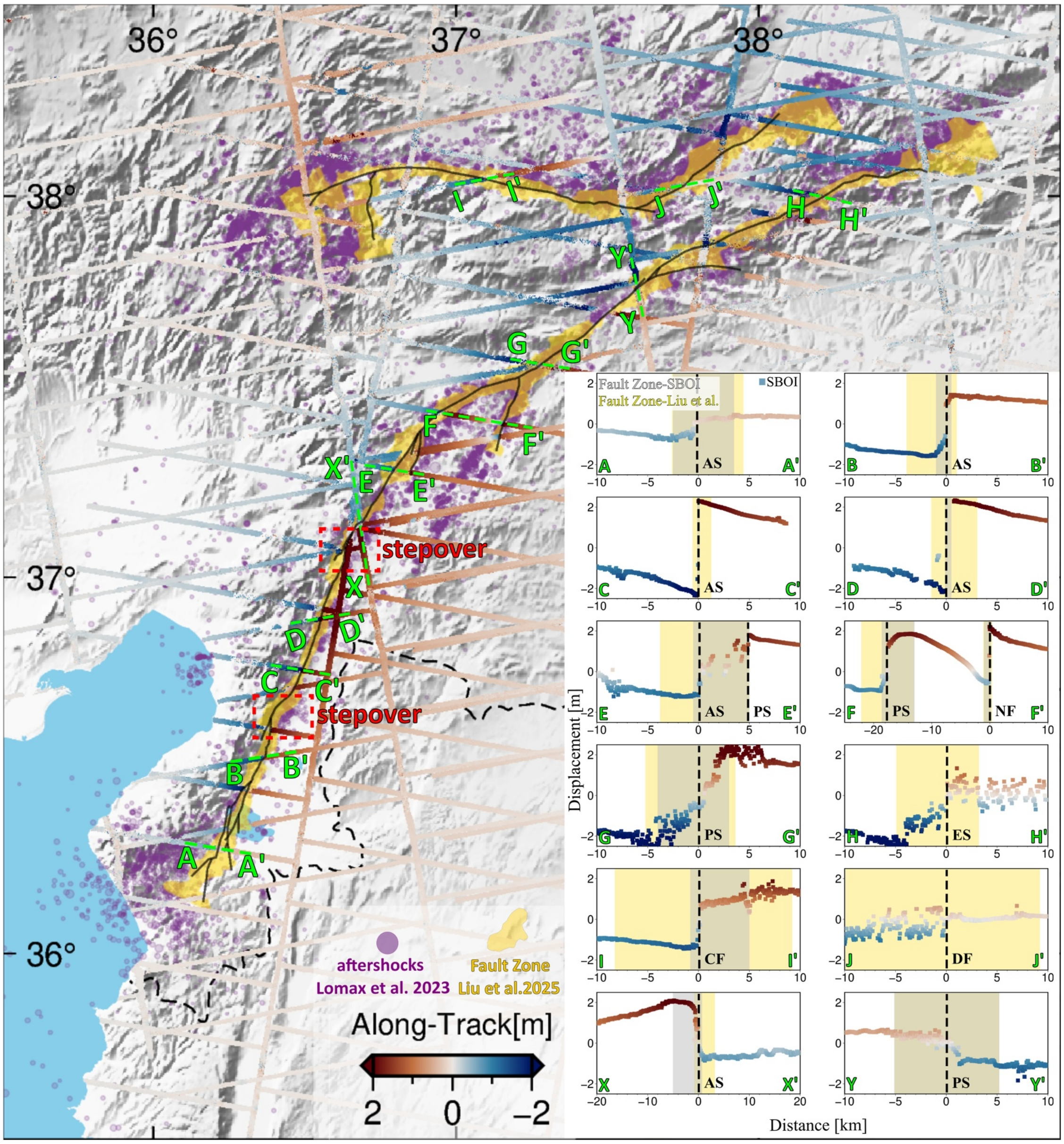

Figure 13. SBOI along-track displacement profiles across the 2023 earthquake rupture. Green dashed lines indicate the locations of the SBOI profiles, with Profiles A–J derived from burst overlap regions and Profiles X–Y from subswath overlaps, superimposed on the along-track displacement map, with red and blue indicating northward and southward displacements, respectively. Background shading shows the fault zone width from J. Liu et al. (2025) (yellow), interpreted as zones of distributed off-fault deformation, and aftershock distribution from (Lomax, 2023) (purple dots). The right inset panel presents the corresponding SBOI displacement profiles. Gray shading indicates the fault zone width inferred from the SBOI-based model fits (see Figure S22 in Supporting Information S1), while yellow shading shows the fault zone width from J. Liu et al. (2025) along each SBOI cross-section. Black dashed vertical lines mark the approximate fault locations for each profile, labeled by segment: AS = Amanos Segment, PS = Pazarcık Segment, NF = Narlı Fault, ES = Erkenek Segment, CF = Çardak Fault, DF = Doğanşehir Fault.

limitations from decorrelation (e.g., snowfall, vegetation) and sparse data in overlap zones, SBOI offers critical insights into the spatial variability of rupture processes and damage zone characteristics.

5. Conclusions

This study demonstrates the potential of Subswath and Burst Overlap Interferometry (SBOI) in effectively utilizing all overlap areas in both azimuth and range directions of Sentinel-1 TOPS mode for along-track deformation extraction. By calculating pixel-based scaling factors, the varying precision of overlap regions can be handled systematically.

Our results highlight SBOI's ability to retrieve near-field deformation in high-gradient displacement zones, where traditional InSAR/SAR methods often fail due to decorrelation or limited precision, as observed during the 2023 Kahramanmaraş Earthquakes. Specifically, SBOI significantly enhanced the north-south component of the 3D displacement field and improved slip inversion results along the East Anatolian Fault and Çardak-Sürgü Fault. These advancements provide better constraints on fault slip distributions across both shallow and deep fault segments.

The integration of SBOI data into the COMET-LiCS portal (Lazeckỳ et al., 2023) marks a critical step toward broader accessibility for researchers, enabling deformation analyses for coseismic, postseismic, and interseismic studies. SBOI's ability to resolve high-gradient zones enhances geodetic workflows, offering deeper insights into fault mechanics, seismic hazard assessment, and related deformation processes.

Future work will focus on advancing data processing techniques, including noise reduction strategies such as corrections for ionospheric effects and solid Earth tides, to further enhance SBOI's precision and applicability. Beyond earthquake deformation, SBOI holds great potential for monitoring other geophysical processes, such as volcanic activity and landslides, which are critical for constraining north-south deformation. Additionally, long-term time series analysis will enable effective monitoring of interseismic deformation and postseismic processes, providing deeper insights into fault behavior, fault geometry, seismic hazard management, and broader tectonic processes.

In conclusion, SBOI is a powerful tool for geodetic studies, complementing existing approaches for deformation analysis and contributing to a better understanding of seismic hazards and Earth's dynamic processes.

Conflict of Interest

The authors declare no conflicts of interest relevant to this study.

Data Availability Statement

The original Pixel Offset Tracking and SBOI results are available on the COMET-LiCS portal (COMET-LiCS, 2025). The SBOI processing codes are implemented in GAMMA software (GAMMA Remote Sensing, 2025) and integrated into the COMET-LiCSAR processing chain (COMET-LiCSAR, 2025). The GBISv2.1 geodetic slip inversion software is available on Zenodo (Hooper & Nergizci, 2025). The 3D displacement field and coseismic slip model derived from all data sets are available on Zenodo (Nergizci et al., 2025).

Acknowledgments

This work was supported by the Natural Environment Research Council (NERC) large Grant, “Looking Inside the Continents from Space” (NE/K010867/1). COMET is the NERC Centre for the Observation and Modelling of Earthquakes, Volcanoes, and Tectonics, a partnership between UK universities and the British Geological Survey. The first author is funded by the Republic of Türkiye Ministry of National Education during his PhD studies. The first author extends his gratitude to Dr. Yuan Gao, Dr. Jin Fang, and Dr. Zhen Li from the University of Leeds, as well as Dr. Zhangfeng Ma from the Earth Observatory of Singapore, for their valuable discussions and insights during the preparation of this paper. The authors would also like to thank the three anonymous reviewers and the Associate Editor for their constructive feedback, which greatly improved the clarity and quality of the manuscript. The Sentinel-1 data were analyzed by COMET LiCSAR system at JASMIN, the UK's collaborative data analysis environment (https://jasmin.ac.uk) and Geodetic slip inversion was undertaken on ARC4 and AIRE, High Performance Computing facilities at the University of Leeds, UK (https://arcdocs.leeds.ac.uk/welcome.html). Figures were produced using Matlab, Python, PyGMT (Uieda et al., 2021; Wessel et al., 2013) and Inkscape.

References

Antoine, S. L., Klinger, Y., Delorme, A., Wang, K., Bürgmann, R., & Gold, R. D. (2021). Diffuse deformation and surface faulting distribution from submetric image correlation along the 2019 Ridgecrest, California, ruptures. *Bulletin of the Seismological Society of America*, *111*(5), 2275–2302. https://doi.org/10.1785/0120210036

Bagnardi, M., & Hooper, A. (2018). Inversion of surface deformation data for rapid estimates of source parameters and uncertainties: A Bayesian approach. *Geochemistry, Geophysics, Geosystems*, *19*(7), 2194–2211. https://doi.org/10.1029/2018gc007585

Barbot, S., Luo, H., Wang, T., Hamiel, Y., Piatibratova, O., Javed, M. T., et al. (2023). Slip distribution of the February 6, 2023 mw 7.8 and mw 7.6, Kahramanmaraş, Turkey earthquake sequence in the East Anatolian fault zone. *Seismica*, *2*(3). https://doi.org/10.26443/seismica.v2i3.502

Bechor, N. B., & Zebker, H. A. (2006). Measuring two-dimensional movements using a single InSAR pair. *Geophysical Research Letters*, *33*(16). https://doi.org/10.1029/2006gl026883

Ben-Zion, Y., & Sammis, C. G. (2003). Characterization of fault zones. *Pure and Applied Geophysics*, *160*(3), 677–715. https://doi.org/10.1007/pl00012554

Biggs, J., & Wright, T. J. (2020). How satellite InSAR has grown from opportunistic science to routine monitoring over the last decade. *Nature Communications*, *11*(1), 3863. https://doi.org/10.1038/s41467-020-17587-6

Brcic, R., Yague-Martinez, N., Rodriguez-Gonzalez, F., Shau, R., & Sakar, N. (2014). Sentinel-1 interferometry using the integrated wide area processor (IWAP) – First experiences. In *Sentinel-1 InSARAP workshop*. Retrieved from https://seom.esa.int/insarap/files/INSARAP-2014_Brcic.pdf

Bürgmann, R., Rosen, P. A., & Fielding, E. J. (2000). Synthetic aperture radar interferometry to measure Earth's surface topography and its deformation. *Annual Review of Earth and Planetary Sciences*, *28*(1), 169–209. https://doi.org/10.1146/annurev.earth.28.1.169

Chen, C. W., & Zebker, H. A. (2001). Two-dimensional phase unwrapping with use of statistical models for cost functions in nonlinear optimization. *JOSA A*, *18*(2), 338–351. https://doi.org/10.1364/josaa.18.000338

Chester, F., & Logan, J. M. (1986). Implications for mechanical properties of brittle faults from observations of the punchbowl fault zone, California. *Pure and Applied Geophysics*, *124*(1), 79–106. https://doi.org/10.1007/bf00875720

COMET-LiCS. (2025). COMET-LiCS portal [Dataset]. https://comet.nerc.ac.uk/comet-lics-portal/

COMET-LiCSAR. (2025). COMET-LiCSAR processing chain [Software]. https://github.com/comet-licsar/licsar_proc

Cui, Y., Ma, Z., Aoki, Y., Liu, J., Yue, D., Hu, J., et al. (2022). Refining slip distribution in moderate earthquakes using Sentinel-1 burst overlap interferometry: A case study over 2020 May 15 m w 6.5 Monte Cristo Range Earthquake. *Geophysical Journal International*, *229*(1), 472–486. https://doi.org/10.1093/gji/ggab492

Davidson, G., Mantle, V., Rabus, B., Williams, D., & Geudtner, D. (2013). Implementation of TOPS mode on RADARSAT-2 in support of the Sentinel-1 mission. In *Proc. living planet symposium* (pp. 1–22).

Dor, O., Rockwell, T. K., & Ben-Zion, Y. (2006). Geological observations of damage asymmetry in the structure of the San Jacinto, San Andreas and punchbowl faults in southern California: A possible indicator for preferred rupture propagation direction. *Pure and Applied Geophysics*, *163*(2), 301–349. https://doi.org/10.1007/s00024-005-0023-9

Elliott, J., Walters, R., & Wright, T. (2016). The role of space-based observation in understanding and responding to active tectonics and earthquakes. *Nature Communications*, *7*(1), 13844. https://doi.org/10.1038/ncomms13844

Emre, Ö., Duman, T. Y., Özalp, S., Şaroğlu, F., Olgun, Ş., Elmacı, H., & Çan, T. (2018). Active fault database of Turkey. *Bulletin of Earthquake Engineering*, *16*(8), 3229–3275. https://doi.org/10.1007/s10518-016-0041-2

Fang, J., Ou, Q., Wright, T. J., Okuwaki, R., Amey, R. M., Craig, T. J., et al. (2022). Earthquake cycle deformation associated with the 2021 M_W 7.4 Maduo (Eastern Tibet) earthquake: An intrablock rupture event on a slow-slipping fault from sentinel-1 InSAR and teleseismic data. *Journal of Geophysical Research: Solid Earth*, *127*(11), e2022JB024268. https://doi.org/10.1029/2022jb024268

Fialko, Y., Simons, M., & Agnew, D. (2001). The complete (3-D) surface displacement field in the epicentral area of the 1999 M_W7. 1 hector mine earthquake, California, from space geodetic observations. *Geophysical Research Letters*, *28*(16), 3063–3066. https://doi.org/10.1029/2001gl013174

Fielding, E. J., Lundgren, P. R., Taymaz, T., Yolsal-Çevikbilen, S., & Owen, S. E. (2013). Fault-slip source models for the 2011 M 7.1 Van earthquake in Turkey from SAR interferometry, pixel offset tracking, GPS, and seismic waveform analysis. *Seismological Research Letters*, *84*(4), 579–593. https://doi.org/10.1785/0220120164

Funning, G. J., Parsons, B., Wright, T. J., Jackson, J. A., & Fielding, E. J. (2005). Surface displacements and source parameters of the 2003 Bam (Iran) earthquake from Envisat advanced synthetic aperture radar imagery. *Journal of Geophysical Research*, *110*(B9). https://doi.org/10.1029/2004jb003338

GAMMA Remote Sensing. (2025). Gamma software. Retrieved from https://gamma-rs.ch/gamma-software

Geudtner, D. (2014). Implementation of the TOPS mode on RADARSAT-2 in support of the Copernicus Sentinel-1 mission: RADARSAT-2 TOPS SAR interferometry (InSAR) scene pair data acquisitions. *ESA reference S1-TN-ESA-SY*, 452.

Gomba, G., González, F. R., & De Zan, F. (2016). Ionospheric phase screen compensation for the Sentinel-1 TOPS and ALOS-2 ScanSAR modes. *IEEE Transactions on Geoscience and Remote Sensing*, *55*(1), 223–235.

Grandin, R., Klein, E., Métois, M., & Vigny, C. (2016). Three-dimensional displacement field of the 2015 M_W8. 3 Illapel earthquake (Chile) from across-and along-track Sentinel-1 TOPS interferometry. *Geophysical Research Letters*, *43*(6), 2552–2561. https://doi.org/10.1002/2016GL067954

Güvercin, S. E., Karabulut, H., Konca, A. Ö., Doğan, U., & Ergintav, S. (2022). Active seismotectonics of the east Anatolian fault. *Geophysical Journal International*, *230*(1), 50–69. https://doi.org/10.1093/gji/ggac045

Hayek, J. N., Marchandon, M., Li, D., Pousse-Beltran, L., Hollingsworth, J., Li, T., & Gabriel, A.-A. (2024). Non-typical supershear rupture: Fault heterogeneity and segmentation govern unilateral supershear and cascading multi-fault rupture in the 2021 m w m_w 7.4 Maduo earthquake. *Geophysical Research Letters*, *51*(20), e2024GL110128. https://doi.org/10.1029/2024gl110128

He, P., Wen, Y., Xu, C., & Chen, Y. (2019a). Complete three-dimensional near-field surface displacements from imaging geodesy techniques applied to the 2016 Kumamoto earthquake. *Remote Sensing of Environment*, *232*, 111321. https://doi.org/10.1016/j.rse.2019.111321

He, P., Wen, Y., Xu, C., & Chen, Y. (2019b). High-quality three-dimensional displacement fields from new-generation SAR imagery: Application to the 2017 Ezgeleh, Iran, earthquake. *Journal of Geodesy*, *93*(4), 573–591. https://doi.org/10.1007/s00190-018-1183-6

Hooper, A., & Nergizci, M. (2025). mnergizci/GBISv2: GBISv2.0.1 (Geodetic Bayesian Inversion Software) [Software]. *Zenodo*. https://doi.org/10.5281/zenodo.14927647

Hooper, A., & Spaans, K. (2016). Sentinel-1 burst overlap InSAR: North-south sensitivity at last? In *AGU fall meeting abstracts* (Vol. 2016). G21C-08

Hu, J., Li, Z., Ding, X., Zhu, J., Zhang, L., & Sun, Q. (2014). Resolving three-dimensional surface displacements from InSAR measurements: A review. *Earth-Science Reviews*, *133*, 1–17. https://doi.org/10.1016/j.earscirev.2014.02.005

Hussain, E., Kalaycıoğlu, S., Milliner, C. W., & Çakir, Z. (2023). Preconditioning the 2023 Kahramanmaraş (Türkiye) earthquake disaster. *Nature Reviews Earth & Environment*, *4*(5), 287–289.

Hussain, E., Wright, T. J., Walters, R. J., Bekaert, D. P., Lloyd, R., & Hooper, A. (2018). Constant strain accumulation rate between major earthquakes on the north Anatolian fault. *Nature Communications*, *9*(1), 1392. https://doi.org/10.1038/s41467-018-03739-2

Jia, Z., Jin, Z., Marchandon, M., Ulrich, T., Gabriel, A.-A., Fan, W., et al. (2023). The complex dynamics of the 2023 Kahramanmaraş, Turkey, m w 7.8-7.7 earthquake doublet. *Science*, *381*(6661), 985–990. https://doi.org/10.1126/science.adi0685

Jiang, H., Feng, G., Wang, T., & Bürgmann, R. (2017). Toward full exploitation of coherent and incoherent information in Sentinel-1 TOPS data for retrieving surface displacement: Application to the 2016 Kumamoto (Japan) earthquake. *Geophysical Research Letters*, *44*(4), 1758–1767. https://doi.org/10.1002/2016gl072253

Jiang, K., Xu, W., & Xie, L. (2024). Unwrap intractable C-band coseismic interferograms: An improved SNAPHU method with range offset gradients as prior information. *Journal of Geophysical Research: Solid Earth*, *129*(10), e2024JB028826. https://doi.org/10.1029/2024jb028826

Jolivet, R., Duputel, Z., Riel, B., Simons, M., Rivera, L., Minson, S., et al. (2014). The 2013 m w 7.7 Balochistan earthquake: Seismic potential of an accretionary wedge. *Bulletin of the Seismological Society of America*, *104*(2), 1020–1030. https://doi.org/10.1785/0120130313

Jung, H.-S., Lee, W.-J., & Zhang, L. (2014). Theoretical accuracy of along-track displacement measurements from Multiple-Aperture Interferometry (MAI). *Sensors*, *14*(9), 17703–17724. https://doi.org/10.3390/s140917703

Karabacak, V., Özkaymak, Ç., Sözbilir, H., Tatar, O., Aktuğ, B., Özdağ, Ö. C., et al. (2023). The 2023 Pazarcık (Kahramanmaraş, Türkiye) earthquake (mw 7.7): Implications for surface rupture dynamics along the east Anatolian fault zone. *The Geological Society of London*, *180*(3), jgs2023-020. https://doi.org/10.1144/jgs2023-020

Lazecký, M., Hooper, A., & Piromthong, P. (2023). InSAR-derived horizontal velocities in a global reference frame. *Geophysical Research Letters*, *50*(10), e2022GL101173. https://doi.org/10.1029/2022gl101173

Lemrabet, L., Doin, M.-p., Lasserre, C., & Durand, P. (2023). Referencing of continental-scale InSAR-derived velocity fields: Case study of the eastern Tibetan plateau. *Journal of Geophysical Research: Solid Earth*, *128*(7), e2022JB026251. https://doi.org/10.1029/2022jb026251

Li, C., Li, T., Hollingsworth, J., Zhang, Y., Qian, L., & Shan, X. (2023). Strain threshold for the formation of coseismic surface rupture. *Geophysical Research Letters*, *50*(16), e2023GL103666. https://doi.org/10.1029/2023gl103666

Li, X., Jónsson, S., & Cao, Y. (2021). Interseismic deformation from Sentinel-1 burst-overlap interferometry: Application to the southern Dead Sea fault. *Geophysical Research Letters*, *48*(16), e2021GL093481. https://doi.org/10.1029/2021gl093481

Li, X., Jónsson, S., Liu, S., Ma, Z., Castro-Perdomo, N., Cesca, S., et al. (2024). Resolving the slip-rate inconsistency of the northern Dead Sea fault. *Science Advances*, *10*(11), eadj8408. https://doi.org/10.1126/sciadv.adj8408

Liang, C., Agram, P., Simons, M., & Fielding, E. J. (2019). Ionospheric correction of InSAR time series analysis of C-band SENTINEL-1 TOPS data. *IEEE Transactions on Geoscience and Remote Sensing*, *57*(9), 6755–6773. https://doi.org/10.1109/tgrs.2019.2908494

Liang, P., Xu, Y., Zhou, X., Li, Y., Tian, Q., Zhang, H., et al. (2024). Coseismic surface ruptures of M_W7. 8 and M_W7.5 earthquakes occurred on February 6, 2023, and seismic hazard assessment of the east Anatolian Fault Zone, Southeastern Türkiye. *Science China Earth Sciences*, *68*(2), 611–625.

Liu, C., Lay, T., Wang, R., Taymaz, T., Xie, Z., Xiong, X., et al. (2023). Complex multi-fault rupture and triggering during the 2023 earthquake doublet in southeastern Türkiye. *Nature Communications*, *14*(1), 5564. https://doi.org/10.1038/s41467-023-41404-5

Liu, J., Hu, J., Li, Z., Ma, Z., Shi, J., Xu, W., & Sun, Q. (2022). Three-dimensional surface displacements of the 8 January 2022 M_W6. 7 Menyuan earthquake, China from Sentinel-1 and ALOS-2 SAR observations. *Remote Sensing*, *14*(6), 1404. https://doi.org/10.3390/rs14061404

Liu, J., Hu, J., Li, Z., Ma, Z., Wu, L., Jiang, W., et al. (2022). Complete three-dimensional coseismic displacements due to the 2021 Maduo earthquake in Qinghai Province, China from Sentinel-1 and ALOS-2 SAR images. *Science China Earth Sciences*, *65*(4), 687–697. https://doi.org/10.1007/s11430-021-9868-9

Liu, J., Jónsson, S., Li, X., Yao, W., & Klinger, Y. (2025). Extensive off-fault damage around the 2023 Kahramanmaraş earthquake surface ruptures. *Nature Communications*, *16*(1), 1286. https://doi.org/10.1038/s41467-025-56466-w

Lohman, R. B., & Simons, M. (2005). Some thoughts on the use of InSAR data to constrain models of surface deformation: Noise structure and data downsampling. *Geochemistry, Geophysics, Geosystems*, *6*(1). https://doi.org/10.1029/2004gc000841

Lomax, A. (2023). Precise, NLL-SSST-coherence hypocenter catalog for the 2023 M_W 7.8 and M_W 7.6 SE Turkey earthquake sequence.

López-Dekker, P., Biggs, J., Chapron, B., Hooper, A., Kääb, A., Masina, S., et al. (2021). The harmony mission: End of phase-0 science overview. In *2021 IEEE international geoscience and remote sensing symposium IGARSS* (pp. 7752–7755).

Lu, S., Liang, C., & Zeng, Q. (2025). Limitations of earthquake coseismic deformation measurements using InSAR. *International Journal of Remote Sensing*, *46*(5), 1–21. https://doi.org/10.1080/01431161.2024.2449478

Ma, Z., Li, C., Jiang, Y., Chen, Y., Yin, X., Aoki, Y., et al. (2024). Space geodetic insights to the dramatic stress rotation induced by the February 2023 Turkey-Syria earthquake doublet. *Geophysical Research Letters*, *51*(6), e2023GL107788. https://doi.org/10.1029/2023gl107788

Ma, Z., Wei, S.-J., Li, X., Aoki, Y., Liu, J.-H., Liu, X.-J., et al. (2022). Challenges and prospects to time series burst overlap interferometry (BOI): Some insights from a new BOI algorithm test over the Chaman fault. *IEEE Transactions on Geoscience and Remote Sensing*, *60*, 1–19.

Magen, Y., Baer, G., Ziv, A., Inbal, A., & Nof, R. (2024). The postseismic deformation of the 6 July 2019 M_W 7.1 Ridgecrest earthquake from burst overlap interferometry, InSAR, and GNSS. *Seismological Research Letters*, *96*(2A), 868–882. https://doi.org/10.1785/0220240066

Magen, Y., Baer, G., Ziv, A., Inbal, A., Nof, R. N., Hamiel, Y., et al. (2024). Fault coalescence, slip distribution, and stress drop of the February 2023 southeast Türkiye earthquakes from joint inversion of SAR, GNSS, and burst overlap interferometry. *Seismological Research Letters*, *95*(2A), 680–696. https://doi.org/10.1785/0220230271

Melgar, D., Taymaz, T., Ganas, A., Crowell, B. W., Öcalan, T., Kahraman, M., et al. (2023). Sub-and super-shear ruptures during the 2023 M_W 7.8 and M_W 7.6 earthquake doublet in SE Türkiye. https://doi.org/10.26443/seismica.v2i3.387

Meng, J., Kusky, T., Mooney, W. D., Bozkurt, E., Bodur, M. N., & Wang, L. (2024). Surface deformations of the 6 February 2023 earthquake sequence, eastern Türkiye. *Science*, *383*(6680), 298–305. https://doi.org/10.1126/science.adj3770

Merryman, B., & Peter, J. (2019). Measuring coseismic deformation with spaceborne synthetic aperture radar: A review. *Frontiers in Earth Science*, *7*, 16. https://doi.org/10.3389/feart.2019.00016

Meta, A., Mittermayer, J., Prats, P., Scheiber, R., & Steinbrecher, U. (2009). TOPS imaging with TerraSAR-X: Mode design and performance analysis. *IEEE Transactions on Geoscience and Remote Sensing*, *48*(2), 759–769. https://doi.org/10.1109/tgrs.2009.2026743

Michel, R., Avouac, J.-P., & Taboury, J. (1999). Measuring ground displacements from SAR amplitude images: Application to the landers earthquake. *Geophysical Research Letters*, *26*(7), 875–878. https://doi.org/10.1029/1999gl900138

Milliner, C. W., Dolan, J. F., Hollingsworth, J., Leprince, S., Ayoub, F., & Sammis, C. G. (2015). Quantifying near-field and off-fault deformation patterns of the 1992 M_W 7.3 1 Anders earthquake. *Geochemistry, Geophysics, Geosystems*, *16*(5), 1577–1598. https://doi.org/10.1002/2014gc005693

Mitchell, T., & Faulkner, D. (2009). The nature and origin of off-fault damage surrounding strike-slip fault zones with a wide range of displacements: A field study from the Atacama fault system, northern Chile. *Journal of Structural Geology*, *31*(8), 802–816. https://doi.org/10.1016/j.jsg.2009.05.002

Morishita, Y., & Kobayashi, T. (2022). Three-dimensional deformation and its uncertainty derived by integrating multiple SAR data analysis methods. *Earth Planets and Space*, *74*(1), 16. https://doi.org/10.1186/s40623-022-01571-z

MTA. (2025). Maden tetkik ve Arama Genel Müdürlüğü Yerbilimleri Harita Görüntüleyici. Retrieved from https://yerbilimleri.mta.gov.tr/anasayfa.aspx

Nergizci, M., Lazecky, M., Ou, Q., Wright, T. J., Hooper, A., Magnard, C., & Cakir, Z. (2025). Refining 3D displacement fields and Coseismic Slip Models of the 2023 Kahramanmaras Earthquakes using Subswath and Burst Overlap Interferometry (SBOI) [Dataset]. *Zenodo*. https://doi.org/10.5281/zenodo.14927371

Okada, Y. (1985). Surface deformation due to shear and tensile faults in a half-space. *Bulletin of the Seismological Society of America*, *75*(4), 1135–1154. https://doi.org/10.1785/bssa0750041135

Ou, Q., Daout, S., Weiss, J., Shen, L., Lazeckỳ, M., Wright, T. J., & Parsons, B. E. (2022). Large-scale interseismic strain mapping of the NE Tibetan plateau from Sentinel-1 interferometry. *Journal of Geophysical Research: Solid Earth*, *127*(6), e2022JB024176. https://doi.org/10.1029/2022jb024176

Özkan, A., Solak, H. İ., Tiryakioğlu, İ., Şentürk, M. D., Aktuğ, B., Gezgin, C., et al. (2023). Characterization of the co-seismic pattern and slip distribution of the February 06, 2023, Kahramanmaraş (Turkey) earthquakes (M_W 7.7 and M_W 7.6) with a dense GNSS network. *Tectonophysics*, *866*, 230041. https://doi.org/10.1016/j.tecto.2023.230041

Pappas, O., Biggs, J., Prats-Iraola, P., Pulella, A., Stinton, A., & Achim, A. (2025). Measuring topographic change after volcanic eruptions using multistatic SAR satellites: Simulations in preparation for ESA's harmony mission. *Remote Sensing of Environment*, *317*, 114528. https://doi.org/10.1016/j.rse.2024.114528

Perna, S., Longo, F., Zoffoli, S., Davidson, M., Iannini, L., & Lanari, R. (2024). Enabling the forthcoming ROSE-L sensor for a two-look ScanSAR mode configuration without modifying the system parameters. In *EUSAR 2024; 15th European conference on synthetic aperture radar* (pp. 827–832).

Perrin, C., Manighetti, I., Ampuero, J.-P., Cappa, F., & Gaudemer, Y. (2016). Location of largest earthquake slip and fast rupture controlled by along-strike change in fault structural maturity due to fault growth. *Journal of Geophysical Research: Solid Earth*, *121*(5), 3666–3685. https://doi.org/10.1002/2015jb012671

Piromthong, P., & Hooper, A. (2025). Ionospheric mitigation for InSAR and BOI using a time-series approach. *Authorea Preprints*.

Prats-Iraola, P., Scheiber, R., Marotti, L., Wollstadt, S., & Reigber, A. (2012). TOPS interferometry with TerraSAR-X. *IEEE Transactions on Geoscience and Remote Sensing*, *50*(8), 3179–3188. https://doi.org/10.1109/TGRS.2011.2178247

Provost, F., Karabacak, V., Malet, J.-P., Van der Woerd, J., Meghraoui, M., Masson, F., et al. (2024). High-resolution co-seismic fault offsets of the 2023 Türkiye earthquake ruptures using satellite imagery. *Scientific Reports*, *14*(1), 6834. https://doi.org/10.1038/s41598-024-55009-5

Pucci, S., Caciagli, M., Azzaro, R., Di Manna, P., Blumetti, A. M., Poggi, V., et al. (2025). Examples of rupture patterns of the 2023, M_W 7.8 Kahramanmaraş surface-faulting earthquake, Türkiye. *Geosciences*.

Ren, C., Wang, Z., Taymaz, T., Hu, N., Luo, H., Zhao, Z., et al. (2024). Supershear triggering and cascading fault ruptures of the 2023 Kahramanmaraş, Türkiye, earthquake doublet. *Science*, *383*(6680), 305–311. https://doi.org/10.1126/science.adi1519

Rodriguez-Cassola, M., Prats-Iraola, P., De Zan, F., Scheiber, R., Reigber, A., Geudtner, D., & Moreira, A. (2014). Doppler-related distortions in TOPS SAR images. *IEEE Transactions on Geoscience and Remote Sensing*, *53*(1), 25–35. https://doi.org/10.1109/tgrs.2014.2313068

Rosen, P. A., & Kumar, R. (2021). NASA-ISRO SAR (NISAR) mission status. In *2021 IEEE radar conference (radarconf21)* (pp. 1–6).

Samsonov, S. V., & Jiang, Y. (2024). RADARSAT-2 DinSAR and GNSS-derived finite fault model of the 2012 mw 7.8 Haida Gwaii earthquake. *Canadian Journal of Remote Sensing*, *50*(1), 2424768. https://doi.org/10.1080/07038992.2024.2424768

Savage, J., & Burford, R. (1973). Geodetic determination of relative plate motion in central California. *Journal of Geophysical Research*, *78*(5), 832–845. https://doi.org/10.1029/jb078i005p00832

Scheiber, R., & Moreira, A. (2000). Coregistration of interferometric SAR images using spectral diversity. *IEEE Transactions on Geoscience and Remote Sensing*, *38*(5), 2179–2191. https://doi.org/10.1109/36.868876

Scheiber, R., Wollstadt, S., Sauer, S., Malz, E., Mittermayer, J., Prats, P., et al. (2010). Sentinel-1 imaging performance verification with TerraSAR-X. In *8th European conference on synthetic aperture radar* (pp. 1–4).

Scott, C. P., Arrowsmith, J. R., Nissen, E., Lajoie, L., Maruyama, T., & Chiba, T. (2018). The M7 2016 Kumamoto, Japan, earthquake: 3-D deformation along the fault and within the damage zone constrained from differential lidar topography. *Journal of Geophysical Research: Solid Earth*, *123*(7), 6138–6155. https://doi.org/10.1029/2018jb015581

Shen, L., Hooper, A., Elliott, J. R., & Wright, T. J. (2024). Variability in interseismic strain accumulation rate and style along the Altyn Tagh fault. *Nature Communications*, *15*(1), 6876. https://doi.org/10.1038/s41467-024-51116-z

Spaans, K. H. (2016). *Near-real time volcano monitoring and modelling using radar interferometry* (Unpublished doctoral dissertation). University of Leeds.

Trumpf, S., Prats-Iraola, P., & Moreira, A. (2025). Along-track deformation retrieval performance with the ROSE-L multi-channel SAR system using two-look ScanSAR. *IEEE Transactions on Geoscience and Remote Sensing*, *63*, 1–15. https://doi.org/10.1109/tgrs.2025.3557542

Uieda, L., Tian, D., Leong, W. J., Toney, L., Schlitzer, W., Grund, M., et al. (2021). PyGMT: A python interface for the generic mapping tools.

USGS. (2023). USGS Turkey earthquake emergency response. Retrieved from https://usgs.maps.arcgis.com/apps/webappviewer/index.html?id=5229bb842bd64b688d769abbefe43b46

Wan, Z., Dong, R., Wang, D., Xu, S., Wang, Z., & Wang, Q. (2024). Along-strike variation of rupture characteristics and aftershock patterns of the 2023 M_W 7.8 Türkiye earthquake controlled by fault structure. *Seismological Research Letters*, *95*(4), 2071–2080. https://doi.org/10.1785/0220230378

Wegmüller, U., Werner, C., Strozzi, T., Wiesmann, A., Frey, O., & Santoro, M. (2016). Sentinel-1 support in the gamma software. *Procedia Computer Science*, *100*, 1305–1312. https://doi.org/10.1016/j.procs.2016.09.246

Weiss, J. R., Walters, R. J., Morishita, Y., Wright, T. J., Lazecky, M., Wang, H., et al. (2020). High-resolution surface velocities and strain for Anatolia from Sentinel-1 InSAR and GNSS data. *Geophysical Research Letters*, *47*(17), e2020GL087376. https://doi.org/10.1029/2020gl087376

Wessel, P., Smith, W. H., Scharroo, R., Luis, J., & Wobbe, F. (2013). Generic mapping tools: Improved version released. *Eos, Transactions American Geophysical Union*, *94*(45), 409–410. https://doi.org/10.1002/2013eo450001

Wright, T. J., Parsons, B. E., & Lu, Z. (2004). Toward mapping surface deformation in three dimensions using InSAR. *Geophysical Research Letters*, *31*(1). https://doi.org/10.1029/2003gl018827

Xu, L., Chen, Q., Zhao, J.-J., Liu, X.-W., Xu, Q., & Yang, Y.-H. (2021). An integrated approach for mapping three-dimensional CoSeismic displacement fields from Sentinel-1 TOPS data based on DInSAR, POT, MAI and BOI techniques: Application to the 2021 mw 7.4 maduo earthquake. *Remote Sensing*, *13*(23), 4847. https://doi.org/10.3390/rs13234847

Xu, X., Tong, X., Sandwell, D. T., Milliner, C. W., Dolan, J. F., Hollingsworth, J., et al. (2016). Refining the shallow slip deficit. *Geophysical Journal International*, *204*(3), 1867–1886. https://doi.org/10.1093/gji/ggv563

Yague-Martinez, N. (2020). *Burst-mode wide-swath SAR interferometry for solid Earth monitoring*. (Unpublished doctoral dissertation). DLR-Microwaves and Radar Institute.

Yague-Martinez, N., Prats-Iraola, P., Pinheiro, M., & Jaeger, M. (2019). Exploitation of burst overlapping areas of TOPS data. Application to Sentinel-1. In *IGARSS 2019-2019 IEEE international geoscience and remote sensing symposium* (pp. 2066–2069).

Yague-Martinez, N., Prats-Iraola, P., Wollstadt, S., & Moreira, A. (2019). The 2-look TOPS mode: Design and demonstration with TerraSAR-X. *IEEE Transactions on Geoscience and Remote Sensing*, *57*(10), 7682–7703. https://doi.org/10.1109/TGRS.2019.2915797

Yao, S., & Yang, H. (2025). Rupture phases reveal geometry-related rupture propagation in a natural earthquake. *Science Advances*, *11*(4), eadq0154. https://doi.org/10.1126/sciadv.adq0154

Yun, S.-H., Zebker, H., Segall, P., Hooper, A., & Poland, M. (2007). Interferogram formation in the presence of complex and large deformation. *Geophysical Research Letters*, *34*(12). https://doi.org/10.1029/2007gl029745

Zhang, Y., Tang, X., Liu, D., Taymaz, T., Eken, T., Guo, R., et al. (2023). Geometric controls on cascading rupture of the 2023 Kahramanmaraş earthquake doublet. *Nature Geoscience*, *16*(11), 1054–1060. https://doi.org/10.1038/s41561-023-01283-3

References From the Supporting Information

Jiang, H., Pei, Y., & Li, J. (2017). Sentinel-1 tops interferometry for along-track displacement measurement. In *IOP conference series: Earth and environmental science* (Vol. 57, p. 012019).

Wang, T., & Jónsson, S. (2015). Improved SAR amplitude image offset measurements for deriving three-dimensional coseismic displacements. *IEEE Journal of Selected Topics in Applied Earth Observations and Remote Sensing*, *8*(7), 3271–3278. https://doi.org/10.1109/JSTARS.2014.2387865